Progressive overfilling of readily releasable pool underlies short-term facilitation at recurrent excitatory synapses in layer 2/3 of the rat prefrontal cortex

Jiwoo Shin[1,2], Seung Yeon Lee[2], Yujin Kim[1,2*], Suk-Ho Lee[1,2,*].

1. Department of Brain and Cognitive Science, College of Natural Sciences, Seoul National University. 2. Department of Physiology, Seoul National University College of Medicine. 03080, Seoul, South Korea.

* *corresponding authors*

Yujin Kim Ph.D. (kim.y@snu.ac.kr)
Cell Physiology Lab
Department of Physiology
Seoul National Univ. College of Medicine

Suk-Ho Lee M.D., Ph.D. (leesukho@snu.ac.kr)
Cell Physiology Lab
Department of Physiology
Seoul National Univ. College of Medicine
103 Daehakro, 03080, Seoul, South Korea
Phone) +82-2-740-8222

Abstract

Short-term facilitation of recurrent excitatory synapses within the cortical network has been proposed to support persistent activity during working memory tasks, yet the underlying mechanisms remain poorly understood. We characterized short-term plasticity at the local excitatory synapses in layer 2/3 of the rat medial prefrontal cortex and studied its presynaptic mechanisms. Low-frequency stimulation induced slowly developing facilitation, whereas high-frequency stimulation initially induced strong depression followed by rapid facilitation. This non-monotonic delayed facilitation after a brief depression resulted from a high vesicular fusion probability and slow activation of Ca^{2+}-dependent vesicle replenishment, which led to the overfilling of release sites beyond their basal occupancy. Pharmacological and gene knockdown (KD) experiments revealed that the facilitation was mediated by phospholipase C/diacylglycerol signaling and synaptotagmin 7 (Syt7). Notably, Syt7 KD abolished facilitation and slowed the refilling rate of vesicles with high fusion probability. Furthermore, Syt7 deficiency in layer 2/3 pyramidal neurons impaired the acquisition of trace fear memory and reduced c-Fos activity. In conclusion, Ca^{2+}- and Syt7-dependent overfilling of release sites mediates synaptic facilitation at L2/3 recurrent excitatory synapses and contributes to temporal associative learning.

Introduction

Synapses in the mammalian central nervous system undergo activity-dependent modulation of synaptic weight during repetitive stimulation, known as short-term synaptic plasticity (STP). STP is mediated by presynaptic mechanisms that regulate the release probability (p_r), size of the readily releasable pool (RRP), and kinetics of vesicle replenishment of RRP (Zucker and Regehr, 2002; Jackman and Regehr, 2017; Neher and Brose, 2018). Short-term depression has been observed at synapses with a high baseline p_r, primarily because of the rapid depletion of releasable vesicles during high-frequency stimulation (HFS) (Lin et al., 2022). Conversely, vesicle depletion is less pronounced at synapses with a low baseline p_r, and cumulative increases in p_r during HFS are considered to mediate short-term facilitation (Rozov et al., 2001; Pan and Zucker, 2009; Aldahabi et al., 2024). Central synapses exhibit a wide spectrum of STP depending on different combinations of presynaptic factors mediating short-term depression and facilitation.

Previously, facilitation was modeled as an increase in p_r after an action potential (AP) and its slow decay during the inter-spike interval (ISI), resulting in a cumulative increase in p_r during HFS (Markram et al., 1998; Dittman et al., 2000). Recent studies have suggested that the number of docking (or release) sites in an active zone is limited and only partially occupied by releasable vesicles in the resting states (Miki et al., 2016; Pulido and Marty, 2018; Malagon et al., 2020; Lin et al., 2022). Therefore, p_r is determined by the vesicular fusion probability (p_v) and release site occupancy (p_{occ}). However, distinguishing the individual contributions of p_v and p_{occ} to p_r is challenging (Silva et al., 2021; Neher, 2024). It is also unclear whether facilitation is mediated by activity-dependent increases in the p_v, p_{occ}, or both.

63 Two recent models for vesicle priming and release view the 'priming' as a two-step reversible
64 process that leads to a release-ready state. The release-ready vesicles could be vesicles in a
65 tightly docked state (TS) or those occupying specialized docking sites (DS), and are supplied
66 from vesicles in a loosely docked state (LS) or those occupying a distinct replacement sites
67 (RS), which are called LS/TS model ((Neher, 2024); (Aldahabi et al., 2024)) and RS/DS model
68 ((Miki et al., 2016); (Silva et al., 2021)), respectively. Common to both models is the
69 assumption that release-ready vesicles constitute only a fraction of all docked vesicles under
70 resting conditions and that this fraction is up- and down-regulated by synaptic activity.
71 Synaptotagmin-7 (Syt7) was recently found to play a crucial role in facilitation at different
72 types of central synapses (Jackman et al., 2016; Chen et al., 2017; Martinetti et al., 2022). In
73 addition to its role in facilitation, Syt7 accelerates refilling of the RRP after depletion and
74 mediates asynchronous release (Bacaj et al., 2013; Liu et al., 2014; Jackman et al., 2016;
75 Tawfik et al., 2021). Syt7-dependent synaptic facilitation is interpreted as an activity-
76 dependent increase in p_v (Turecek et al., 2016; Jackman and Regehr, 2017; Turecek et al., 2017;
77 Norman et al., 2023). However, it is unclear whether Syt7 contributes to facilitation through
78 a Ca^{2+}-dependent increase in p_{occ} (i.e., overfilling). Overfilling has been proposed as a
79 mechanism supporting facilitation at the Drosophila neuromuscular junction (Kobbersmed et
80 al., 2020), yet whether this process also occurs at the mammalian central synapses mediated
81 by Syt7 has not been studied.
82 Facilitation at recurrent excitatory synapses in cortical recurrent networks may play a crucial
83 role in maintaining working memory (Mongillo et al., 2008; Mongillo et al., 2012; Hansel and
84 Mato, 2013). Although layer 2/3 (L2/3) pyramidal cells (PCs) are highly interconnected and

85 represent task-relevant information during a delay period in working memory tasks (Fujisawa
86 et al., 2008; Ozdemir et al., 2020), most studies on local excitatory recurrent synapses in the
87 neocortex have focused on layer 5 (L5) exhibiting short-term depression (Reyes and Sakmann,
88 1999; Hempel et al., 2000; Yoon et al., 2020). Further, the synaptic properties of excitatory
89 synapses in L2/3 remain poorly understood.
90 In the present study, we found that HFS of local excitatory synapses in L2/3 of the medial
91 prefrontal cortex (mPFC) induced initial strong depression followed by delayed facilitation,
92 whereas low-frequency stimulation induced slow monotonous facilitation. This unique form
93 of STP could be explained by 1) high p_v of RRP vesicles at rest and throughout a train
94 stimulation; 2) the low resting vesicular occupancy of RRP and its activity-dependent increase.
95 These conditions led to delayed facilitation through progressive overfilling of release sites
96 during HFS with high p_v vesicles beyond the resting occupancy. Syt7 knockdown (KD) in L2/3
97 PCs completely abolished these synaptic enhancements by inhibiting the Ca^{2+}-dependent
98 increase in release site occupancy. Finally, behavioral tests for trace fear conditioning showed
99 that Syt7 KD impaired the acquisition of trace fear memory and reduced c-Fos expression in
100 the mPFC. Collectively, these results support that Ca^{2+}- and Syt7-dependent overfilling of
101 release sites mediates synaptic facilitation at L2/3 recurrent excitatory synapses and
102 contributes to temporal associative learning.
103

Results

Frequency dependence of STP at local excitatory synapses in L2/3 of the prelimbic cortex

We examined STP profiles at recurrent excitatory synapses between L2/3 PCs and at synapses from L2/3-PCs to fast-spiking interneurons (FSINs) in the prelimbic area of the rat mPFC. The PCs and FSINs were identified based on their distinct intrinsic properties and morphologies (Fig. S1). To stimulate presynaptic PCs, L2/3 PCs were transfected with a plasmid encoding oChIEF using *in utero* electroporation (IUE; Fig. 1A; Lee et al., 2024). Photostimulation of the oChIEF-expressing cell soma at 40 Hz consistently evoked single APs with high fidelity throughout the 600-pulse trains (Fig. S2A-B), which was consistent with little use-dependent inactivation of oChIEF (Lin et al., 2009; Hass and Glickfeld, 2016).

Given that IUE transfected approximately 10-20% of L2/3 PCs (Fig. 1A), we made a whole-cell patch on a non-transfected L2/3 PC or an FSIN (Fig. 1C). To stimulate a minimal number of excitatory axon fibers, EPSCs were evoked using minimal optical stimulation (Fig. S3A; 470 nm, 3-4 µm in radius and 3-5 ms in duration). EPSCs evoked by minimal stimulation were examined to determine the uniformity of the kinetic properties (Fig. S3B-C). Moreover, we reassessed the kinetics of EPSCs during trains *post hoc* to ensure uniformity. EPSCs were evoked by 20-pulse trains at 4 different frequencies (5, 10, 20, and 40 Hz) to cover the range of firing rates of PCs observed *in vivo* during working memory tasks (Baeg et al., 2003). Excitatory synapses from PCs onto both other PCs and FSINs (PC–PC and PC–FSIN) showed strong (~2-fold enhancement) and lasting (several seconds) short-term facilitation at 20 Hz and lower

124 frequencies (Fig. 1D-E). The PC-PC synapses exhibited stronger facilitation than did the PC-
125 FSIN synapses.
126 Steady-state EPSCs at the PC-PC synapses were not significantly different from 5 to 20 Hz (Fig.
127 1F). Frequency invariance at the PC-PC synapses suggests that Ca^{2+}-dependent synaptic
128 facilitation may counteract vesicle depletion in a frequency-dependent manner (Turecek et
129 al., 2017; Lin et al., 2022). Despite facilitation at all frequencies, the paired pulse ratio (PPR)
130 rapidly decreased as the ISI decreased (Fig. 1G, I). At 40 Hz stimulation, both PC-PC and PC-
131 FSIN synapses initially underwent strong depression then followed by facilitation in a few
132 stimuli (Fig. 1Dd, Ed). Such delayed facilitation after paired pulse depression (PPD) has not
133 been previously observed in central synapses except for a slight increase in EPSC at the
134 cerebellar synapses under artificially depolarized conditions (Pulido and Marty, 2018).
135 We confirmed that optically evoked EPSCs were strictly dependent on AP generation (Fig.
136 S4A), suggesting that EPSCs are evoked by optical stimulation of presynaptic axon fibers
137 rather than by direct depolarization of presynaptic boutons. Additionally, dual patch-clamp
138 techniques showed that the STP of optically evoked EPSCs did not differ from the electrically
139 evoked STP of EPSCs at the PC-FSIN synapses (Fig. S4B). Finally, we confirmed that AMPA
140 receptor (AMPAR) desensitization was not responsible for PPD at 40 Hz, ruling out the
141 possible effects of postsynaptic factors on STP (Fig. S5A), and that AMPAR saturation was not
142 significant during facilitation (Fig. S5B).
143

144 *Delayed facilitation results from slow activation of Ca^{2+}-dependent vesicle replenishment at a*
145 *constantly high vesicular fusion probability*

146 The strong PPD at 40 Hz suggests a high vesicular fusion probability (p_v) and likely tight
147 coupling of the releasable vesicles to a Ca^{2+} source. To test this hypothesis, we examined the
148 effects of EGTA, a slow calcium chelator, on synaptic transmission at the PC-PC synapses. The
149 baseline EPSC amplitude ($EPSC_1$) was not affected by incubation of the slice in the bath
150 solution containing 50 µM EGTA-AM for longer than 20 min, supporting tight coupling.
151 Moreover, the PPR was decreased to 0.19, and subsequent facilitation slowed but was still
152 distinct (Fig. 2A-B). These findings indicate that the initial p_v should be higher than 0.81
153 considering vesicle recruitment during ISI. The effects of EGTA-AM were confirmed in the
154 same cell by measuring the baseline EPSC and PPR before and after applying EGTA-AM to the
155 bath. $EPSC_1$ remained unchanged, while PPR was reduced by half (Fig. S6).
156 Notably, the application of EGTA-AM markedly slowed facilitation at 40 Hz (Fig. 2A,C). The
157 frequency invariance of steady-state EPSCs (Fig. 1F) and the slower facilitation at 40 Hz in the
158 presence of EGTA (Fig. 2A) imply a Ca^{2+}-dependent increase in the refilling rate of the RRP
159 and/or an increase in the p_v of reluctant vesicles in light of previous studies (Hosoi et al., 2007;
160 Liu et al., 2014; Ritzau-Jost et al., 2014; Turecek et al., 2016; Ritzau-Jost et al., 2018; Kusick et
161 al., 2020). Moreover, facilitation was accelerated at higher stimulation frequencies. The plot
162 of the rate constant for the increase in EPSCs (denoted as $\mathbf{k}_{STF}$, the rate constant for the
163 development of short-term facilitation) as a function of the stimulation frequency (f_{stim})
164 revealed a linear relationship (Fig. 2C). $\mathbf{k}_{STF}$ in the presence of EGTA-AM was distinctly below
165 this relationship, supporting the Ca^{2+}-dependent acceleration of facilitation.

166 $\mathbf{k}_{STF}$ was also accelerated when the stimulation frequency was increased from 5 Hz to 40 Hz
167 (Fig. 2D; 1.27 ± 0.18/s to 24.27 ± 3.44/s). Notably, the second 40-Hz train stimulation led to
168 strong PPD, followed by accelerated facilitation (Fig. 2D,E). The strong PPD suggests that the
169 vesicular fusion probability kept high during the 5-Hz stimulation, arguing against the
170 possibility for an increase in p_v. Both two-step sequential priming models, LS/TS and RS/DS
171 models, are suitable to interprete our data and we will refer to the different populations of
172 vesicles as TS and LS vesicles, respectively (Taschenberger et al., 2016; Neher and Brose, 2018;
173 Lin et al., 2022; Neher, 2024). Within this framework, vesicles are are released from TS with
174 high p_v both in the resting state and during facilitation, and the delayed facilitation is seen as
175 a result of Ca^{2+}-dependent progressive increase in the occupancy of TS vesicles on docking
176 sites.
177

178 *Release sites have low baseline occupancy and these are increased during facilitation and post-*
179 *tetanic augmentation*

180 Given that p_v was greater than 0.8, the two-fold increase in EPSC during 20 pulse train
181 stimulations could not be explained by an increase in p_v. Recent studies have shown that
182 vesicle release sites (N) are limited in number and are partially occupied at rest (Miki et al.,
183 2016; Pulido and Marty, 2018; Malagon et al., 2020; Lin et al., 2022). Under such a high p_v,
184 two-fold synaptic facilitation should be attributed to an increase in p_{occ}. The vesicle
185 replenishment rate is accelerated during HFS in a Ca^{2+}-dependent manner (Fig.2A-C; Hosoi et
186 al., 2007). This may lead to the overfilling of release sites beyond their basal vesicular

occupancy, which in turn may increase EPSC under high p_v. To test this hypothesis, we determined the quantal parameters at the L2/3 local excitatory synapses. We first measured the quantal size from asynchronous release events after replacing extracellular Ca^{2+} with Sr^{2+}, as previously described (Yoon et al., 2020) (Fig. S7A-B). The mean and coefficient of variance of the quantal sizes were 24 pA and 0.25 at PC-PC synapses, respectively, and were 30 pA and 0.31 at PC-FSIN synapses, (Fig. S7C).

Next, we performed a variance-mean (V-M) analysis of phasic EPSCs at excitatory synapses during train stimulation at 5 Hz and 40 Hz (Scheuss et al., 2002). Applying multiple-probability fluctuation analysis (MPFA) using intra-site quantal variability of 0.2 (Valera et al., 2012), the V-M plot was best fitted by the number of release sites (N) of 5.3 and the quantal size (q) of 25 pA at the PC-PC synapses (Fig. 3A). The p_r for $EPSC_1$ was calculated as 0.32. We performed the same analysis for the PC-FSIN synapses and found N = 5.3, q = 35 pA, and p_r for $EPSC_1$ = 0.31 (Fig. 3B). Our estimate for N was smaller but comparable to the estimate (6.9) at excitatory synapses in L2/3 of the mouse barrel cortex (Holler et al., 2021).

The p_r estimate was clearly smaller than the possible minimum value for p_v (0.81) estimated from the PPR data (Fig. 2B). Given that p_r is a product of p_{occ} and p_v (Neher, 2024), a p_r smaller than p_v indicates the partial occupancy of release sites in the resting state. If synaptic facilitation were mediated by the recruitment of new release sites, it would be accompanied by an increase in the variance of augmented EPSCs (Valera et al., 2012; Kobbersmed et al., 2020). However, the augmented EPSCs during facilitation followed the same parabola in the V-M plot (Fig. 3A,B). Therefore, facilitation appears to be mediated by the progressive overfilling of a finite number of release sites beyond the basal occupancy. In the next section,

209 we show that p_v is close to unity based on a synaptic failure analysis (Fig. S8). Assuming this,
210 the baseline p_r at the first pulse estimated from the fitted parabolic curve can be largely
211 regarded as a baseline p_{occ} (c.a. 30%), and the two-fold increase in EPSCs during facilitation
212 can be attributed to an increase of up to 60% in p_{occ}.
213 We investigated the time course of recovery from facilitation and post-tetanic augmentation
214 (PTA) by applying dual-train stimulations (30 pulses at 40 Hz) separated by different inter-
215 burst intervals (IBIs; Fig. 3C,D). The initial EPSCs in the second train were enhanced by more
216 than twofold, and followed by a strong PPD, suggesting that fusion probability stays high in
217 the IBIs and thus synaptic transmission is carried by TS vesicles. The decay time course of PTA
218 was characterized by two phases (initially fast and later slow; Fig. 3E), which may reflect a
219 two-phase Ca^{2+} decay or two distinct recovery processes that occur sequentially. The variance
220 of potentiated EPSCs measured at IBIs of 0.1, 0.2, and 0.5 s was not different from that of
221 EPSCs at the peak of facilitation (filled circles, Fig. 3A-B). Given that the same RRP mediates
222 both facilitation and augmentation and that post-tetanic EPSCs is carried by TS vesicles similar
223 to the baseline EPSCs, this plot suggests that PTA, similar to short-term facilitation, is
224 mediated by an increase in the TS vesicle occupancy.
225

226 *Failure rate analysis suggests that vesicular fusion probability is closed to one*

227 The vesicle dynamics of STP has been explained using a simple refilling model (Hosoi et al.,
228 2007; Neher and Sakaba, 2008). This model assumes that the vesicles are reversibly docked
229 to a limited number of release sites (N) with forward and reverse rate constants (denoted as

230 k_1 and b_1, respectively). Under the framework of the simple refilling model (see *Materials and*
231 *Methods*), the rate constant for the refilling of the RRP after depletion by the first pulse is the
232 sum of the baseline k_1 (k_1) and b_1. This is estimated as 23/s from the plot of PPR as a function
233 of ISIs (Fig. S8A). From the baseline occupancy of 0.3 and $p_{occ} = k_1 / (k_1 + b_1)$, we estimated k_1
234 to be 6.9/s.
235 When paired APs were applied with an ISI of 20 ms, the failure rate at 1st pulse, $P(F_1)$, was
236 10.6%, and the probability of two consecutive failures, $P(F_1, F_2)$, was 6.2% (Fig. S8A). From the
237 equation $P(F_1) = (1 – p_r)^N$, p_r was calculated as 0.312 when N = 6, comparable to p_r (= 0.32)
238 estimated from the V-M analysis (Fig. 3A). We calculated $P(F_1, F_2)$ under the framework of a
239 simple refilling model, with p_v and k_1 set as free parameters and other parameters set
240 according to the following relationships: $P(F_1) = (1 – p_r)^N$, $p_r = p_v \cdot p_{occ}$, and $p_{occ} = k_1 / (k_1 + b_1)$.
241 The calculated values for $P(F_1, F_2)$ and their difference from the observed value (6.2%) are
242 shown in the plane of k_1 *vs*. p_v in Figure S8B-C. As previously mentioned, k_1 was greater than
243 6/s. Under this high k_1 condition, the difference between the calculated and observed values
244 of $P(F_1,F_2)$ was minimal when $p_v = 1$ (Fig. S8C).
245

246 *Pharmacological manipulations reveal specific molecular identities underlying vesicle loading*
247 *processes*

248 Our results suggest that the baseline occupancy of TS vesicles is low and that the activity-
249 dependent progressive overfilling of docking sites with TS vesicles is responsible for short-
250 term facilitation and augmentation. To elucidate the specific molecular link between synaptic

251 enhancement and Ca^{2+}-dependent overfilling, we examined the effects of several drugs
252 known to affect vesicle dynamics. We first examined the roles of phospholipase C (PLC) and
253 diacylglycerol (DAG) by applying 5 μM U73122, a PLC inhibitor, or 20 μM 1-oleoyl-2-acetyl-sn-
254 glycerol (OAG), a DAG analog. The STP at 40 Hz and PTA at 0.5-s interval were examined before
255 and after applying each drug to the bath. For both drugs, the facilitation and augmentation
256 were reduced (Fig. 4A-B). U73122 did not affect the basal EPSC amplitude ($EPSC_1$) but resulted
257 in a stronger PPD, slower facilitation, and lower augmentation (Fig. 4A). These effects of
258 U73122 suggest the involvement of Ca^{2+}-induced PLC activation in progressive overfilling. In
259 contrast, OAG increased $EPSC_1$ while maintaining a pronounced PPD (Fig. 4B), indicating an
260 increase in the TS vesicle pool size. Meanwhile, OAG slowed $\mathbf{k}_{STF}$ and reduced augmentation,
261 indicating occlusion of activity-dependent synaptic facilitation. Phorbol esters and DAG are
262 thought to accelerate priming through Munc13 activation (Rhee et al., 2002; Taschenberger
263 et al., 2016; Aldahabi et al., 2022); they also shorten the bridges that interlink docked vesicles
264 with the active zone (AZ) membrane (Papantoniou et al., 2023). Collectively, these suggest
265 that PLC- and DAG-mediated signaling play a role in the overfilling of docking sites underlying
266 short-term facilitation and augmentation.
267 Although the acceleration of Ca^{2+}-dependent vesicle refilling supports rapid facilitation at 40
268 Hz, the later part of the delayed facilitation underwent a slight depression, which was more
269 pronounced during the second burst (Fig. 3D, Fig. 4). Sustained synaptic transmission is
270 limited by the spatial availability of docking sites because it is undermined by accumulation
271 of exocytic remainings in the presynaptic AZ during HFS (Neher, 2010; Haucke et al., 2011).
272 To verify this, we examined the effects of dynasore (100 μM), a specific inhibitor of

273 endocytosis (Macia et al., 2006). The treatment with dynasore did not influence $EPSC_1$ or the
274 early phase of facilitation, but it exacerbated depression during the later phase and
275 attenuated PTA (Fig. 4C). This suggests that late synaptic transmission during the 40-Hz train
276 is limited by site clearance.
277 Given the involvement of actin polymerization in the multiple steps of vesicle docking and
278 recycling, we examined the effects of 20 μM latrunculin B (LatB), an inhibitor of actin
279 polymerization. The effects of LatB were complicated: (1) $EPSC_1$ was decreased, whereas PPR
280 was increased (Fig. 4Da) and (2) facilitation and augmentation were reduced (Fig. 4Db). The
281 latter effect may result from defects in vesicle replenishment rates, either through the
282 impaired physical movement of vesicles or disrupted site clearance (Sakaba and Neher, 2003;
283 Lee et al., 2012; Hallermann and Silver, 2013; Miki et al., 2016), as Ca^{2+}-dependent vesicle
284 refilling mediates facilitation and augmentation (Figs. 2–3). Meanwhile, the former effect
285 might be attributed to a shift in equilibrium in the priming states towards a loosely docked
286 state (LS) at rest. It is unknown whether actin affects vesicular fusogenicity in neurons,
287 although it facilitates multiple steps of vesicle fusion by enhancing membrane tension in
288 neuroendocrine cells (Wu and Chan, 2022).
289
290 *Short-term facilitation at both types of local excitatory synapses in L2/3 is abolished by Syt7*
291 *knockdown*

292 We examined whether Syt7 mediates facilitation at the PC-PC and PC-FSIN synapses in L2/3
293 of the mPFC. To this end, oChIEF and shRNA against Syt7 (shSyt7) were co-expressed in L2/3
294 PCs using IUE. Syt7 KD resulted in a complete loss of facilitation at all tested stimulation

295 frequencies (Fig. 5A-B). Short-term depression and paired-pulse depression were more
296 pronounced as the stimulation frequency increased, and the frequency invariance of steady-
297 state EPSC was abolished, implying little contribution of Ca^{2+}-dependent vesicle recruitment
298 (Fig. 5C-F). The lack of facilitation could not be attributed to the failure of APs in presynaptic
299 axons, as optical stimulation elicited reliable APs in Syt7 KD PCs during the 40-Hz train (Fig.
300 S2C). Syt7 KD had little effect on the basal properties, including the peak amplitude,
301 rise/decay time, and time-to-peak, of single AP-induced EPSCs (Fig. S3D-E). Moreover, Syt7
302 KD did not significantly affect the intrinsic properties of neurons (Fig. S9).
303 To examine whether Syt7 KD had any nonautonomous effects on postsynaptic cells, we
304 measured the quantal size (q) from asynchronous events in the presence of Sr^{2+} and found
305 that the mean quantal size remained unaltered at Syt7 KD synapses (Fig. S7C). This indicated
306 that Syt7 did not influence postsynaptic parameters, including the density and kinetic
307 properties of AMPARs. To test the specificity of shSyt7, we examined whether co-expression
308 of the shRNA-resistant form of Syt7 restored synaptic facilitation in both excitatory synapse
309 types. Presynaptic overexpression of shRNA-resistant Syt7 under the CAG promoter rescued
310 the effect of shRNA at both PC-PC and PC-FSIN synapses (Fig. S10). These results underscore
311 the crucial role of presynaptic Syt7 in mediating short-term facilitation at local excitatory
312 synapses in L2/3 of the mPFC.
313

314 *Syt7 KD synapses exhibit complementary changes in the number of release sites and their*
315 *vesicle occupancy*

316 To estimate the quantal parameters in Syt7 KD synapses, we performed V-M analysis of EPSCs
317 evoked by train stimulation (Fig. 6A-B). Fitting a parabola to the V-M plot revealed higher
318 baseline p_{occ} in Syt7 KD synapses than in wild-type (WT) synapses for both synapse types (KD,
319 0.68 and 0.42; WT, 0.32 and 0.31 for PC-PC and PC-FSIN synapses, respectively). The P_{occ}
320 monotonously decreased during a train stimulation, as expected from short-term depression.
321 Moreover, the number of release sites (N) was markedly lower in Syt7 KD synapses (N = 3.5)
322 than in WT synapses (N = 5.3; Fig. 3A). Next, we examined the PTA induced by the same
323 protocol as in Figure 3 (two 40-Hz train stimulations separated by variable IBIs) at Syt7 KD
324 synapses (Fig. 6C). The 40 Hz train-induced synaptic depression quickly recovered during IBIs,
325 but no PTA was observed at Syt7 KD synapses, indicating its crucial role in augmentation (Fig.
326 6D-E).

327

328 *TS vesicle recovery following depletion is accelerated by Syt7*

329 Syt7 is recognized not only for its crucial role in facilitation, but also for mediating Ca^{2+}-
330 dependent replenishment of releasable vesicles (Liu et al., 2014; Tawfik et al., 2021). Given
331 that facilitation at L2/3 excitatory synapses is driven by progressive overfilling (Figs. 2-3), the
332 loss of facilitation at Syt7 KD synapses in the present study implies that Syt7 plays a key role
333 in the Ca^{2+}-dependent acceleration of refilling and overfilling of the docking sites with TS
334 vesicles. To test this hypothesis, we examined the recovery kinetics of EPSCs after TS vesicles
335 were depleted by 3 pulses at 40 Hz in wild-type (WT) and Syt7 KD synapses (Fig. 7). Strong

336 PPD was observed not only in the first burst, but also in the second burst. This suggested that
337 EPSCs in the second burst were mediated by TS vesicles, similar to those in the first burst (Fig.
338 7A,D). Therefore, $EPSC_1$ in the second burst can be interpreted as a release from TS vesicles
339 recovering during a given IBI. The recovery time course of $EPSC_1$ in the second burst indicated
340 full recovery of TS vesicles within 100 ms in both excitatory synapse types in WT rats (Fig.
341 7C,F). However, this recovery was remarkably slower in Syt7 KD synapses, requiring 5 s for
342 full recovery, indicating that TS vesicle recovery was greatly accelerated by Syt7. Overall,
343 synaptic facilitation and augmentation at local excitatory synapses in L2/3 can be ascribed to
344 progressive activity-dependent increases in the occupancy of TS vesicles (Figs. 2-3), in which
345 Syt7 plays a key role.
346

347 *Behavioral consequences of Syt7 KD in L2/3 PCs of the mPFC*

348 We previously proposed that the disparity in STP between the PC-PC and PC-IN synapses
349 results in activity-dependent changes in the ratio of synaptic weights at the PC-PC and PC-IN
350 synapses (J_{ee}/J_{ie}). This may in turn have a profound influence on persistent activity in a
351 recurrent network by biasing the E-I balance (Yoon et al., 2020). Syt7 KD not only eliminated
352 facilitation, but also the activity-dependent increase in the J_{ee}/J_{ie} ratio in the L2/3 network
353 (Fig. S11). This suggests the possibility that Syt7 contributes to the persistent activity during
354 working memory tasks in the L2/3 recurrent network. Trace fear conditioning (tFC) requires
355 associative learning between an auditory cue (conditioned stimulus, CS) and temporally
356 separate aversive events (unconditioned stimulus, US). The formation of trace fear memory

357 requires the prelimbic area of the mPFC and hippocampus. mPFC activity during the trace
358 interval is thought to temporarily hold CS information, enabling the network to associate
359 temporally discontinuous events (i.e., temporal associative learning) (Gilmartin et al., 2013).
360 Synaptic facilitation and augmentation are implicated in temporary memory retention in
361 recurrent networks (Mongillo et al., 2008; Mongillo et al., 2012).
362 Given that Syt7 is crucial for synaptic facilitation (Fig. 5) and augmentation (Fig. 6) in prelimbic
363 L2/3 recurrent excitatory synapses, we tested whether trace fear memory formation was
364 impaired in rats with depleted Syt7 transcripts, specifically in the L2/3 PCs of the mPFC. Syt7-
365 targeted shRNA (shSyt7) or scrambled shRNA (Scr) constructs were transfected bilaterally into
366 the L2/3 PCs of the mPFC using IUE (Fig. 8A). Both the Scr-transfected control and shSyt7-
367 transfected rats underwent tFC training (Fig. 8B). The following day, the rats were subjected
368 to a tone test in which trace fear memory formation was assessed from the freezing response
369 to a tone alone in a distinct context. Compared to the control group, the shSyt7-transfected
370 group exhibited significantly lower levels of freezing behavior in response to auditory cues
371 during the first four trials, suggesting an impairment in trace memory formation (Fig. 8C).
372 The tone test was repeated the following day to test for extinction memory formation. Syt7
373 KD animals exhibited much less freezing to the CS (+1d) than did WT animals. Considering the
374 Rescorla-Wagner model (Yau and McNally, 2023), our results suggest that the strength of CS-
375 US associative memory was weaker in KD animals than in WT animals; thus, the acquisition
376 of trace fear memory was impaired by Syt7 KD in the L2/3 PCs of the mPFC.
377 Next, we assessed the locomotor activity and anxiety levels of rats using the open field test
378 (OFT) and elevated plus maze test (EPM). Scr controls and Syt7 KD rats showed similar

379 exploratory patterns, displaying comparable total distance moved and time spent in the
380 periphery of the OFT or the open/closed arms of the EPM (Fig. S12). Previous studies have
381 suggested that the acquisition of trace fear memory requires elevated trace activity in
382 prelimbic PCs (Gilmartin et al., 2013). Given that c-Fos, an immediate early gene, is
383 upregulated following patterned activities in neurons, its expression is considered a reliable
384 indicator of recent neuronal activation (Fields et al., 1997; Guzowski et al., 2005). To
385 investigate the effect of Syt7 on neuronal activity *in vivo* during tFC, animals were sacrificed
386 at the time of peak c-Fos protein expression, approximately 90 min after completion of the
387 behavioral task (Arime and Akiyama, 2017).
388 To elucidate the activation patterns of specific neuronal populations, we performed
389 immunohistochemical co-labeling of c-Fos and GAD67 (a GABAergic interneuron marker)
390 upon tFC acquisition. The density of c-Fos(+) cells and the percentage of GAD67(+) cells among
391 c-Fos(+) cells in all prelimbic layers were significantly lower in Syt7 KD rats than in control rats
392 (Fig. 8F-G). Additionally, analysis of the proportion of active cells among transfected L2/3 PCs
393 (c-Fos+/GFP+) revealed that Syt7 KD L2/3 PCs were significantly more active than Scr-
394 transfected PCs (Fig. 8H). This unexpected hyperactivity of Syt7 KD PCs may be attributed to
395 the high reciprocal connectivity between PCs and FSINs in the neocortex (Holmgren et al.,
396 2003; Otsuka and Kawaguchi, 2009), as PCs with short-term depression would transmit less
397 input to FSINs, which in turn would exert less feedback inhibition on reciprocally connected
398 PCs. Collectively, these findings show that the slow activation of vesicle refilling supports
399 various forms of facilitation at excitatory synapses in PFC L2/3, which is essential for neuronal
400 activity during temporal associative learning.

401

402 ## Discussion

403 The present study characterized STP at local excitatory synapses in the L2/3 network of the
404 rat mPFC at physiological extracellular [Ca^{2+}]. These synapses displayed initial strong
405 depression and then delayed facilitation at 40 Hz, while monotonous slowly developing
406 facilitation was observed at lower frequencies. Our study suggests that such delayed
407 facilitation after a brief depression results from a high p_v (Figs. 2-3 and Fig. S8), along with
408 Ca^{2+}-dependent delayed acceleration of vesicle refilling and overfilling (Figs. 2–3). The two-
409 fold increase in EPSC during 20 pulse train stimulations under the condition of such a high p_v
410 suggests a Ca^{2+}-dependent increase in the vesicle replenishment rate during a train; this then
411 leads to overfilling of release sites beyond their incomplete basal occupancy (Fig. 3A,B). The
412 high p_v and strong PPD did not result from artificial bouton stimulation, AMPAR
413 desensitization, or any potential distortion caused by optogenetic methods (Figs. S4 and S5).
414 Additionally, similar to short-term facilitation, PTA could be explained by an increase in the
415 TS vesicle occupancy (Fig. 3C-E), consistent with previous studies showing post-tetanic
416 increases in the p_{occ} and/or vesicle pool size at various types of synapses (Lee et al., 2010;
417 Vandael et al., 2020; Tran et al., 2023; Silva et al., 2024). These findings suggest that release
418 sites are partially occupied at rest and that a progressive overfilling of release sites with TS
419 vesicles underlies facilitation and augmentation at intracortical L2/3 excitatory synapses.

420

421 *Progressive overfilling of docking sites*

422 Conventional models for facilitation assume an increase in p_v after an AP of RRP vesicles,
423 which had been in a low_p_v or reluctant state at rest (Dittman et al., 2000; Turecek et al.,
424 2016). This facilitation model is unlikely to explain our results, because TS vesicles are
425 predominantly released not only at rest but also in the facilitated state during or after train
426 stimulation, as evidenced by the strong PPD (ISI, 25 ms) during a 5-Hz train (Fig. 2D-E) and at
427 different intervals after a 40-Hz/30 pulse trains (Fig. 3D). Moreover, the PPD (ISI, 25 ms)
428 remained pronounced during the early phase of facilitation (Fig. 7), arguing against the
429 possibility of slowly increasing the p_v of reluctant vesicles. These results suggested that
430 facilitation was mediated by an activity-dependent progressive increase in occupancy of TS
431 vesicles (TS occupancy). Facilitation through an increase in TS occupancy has been termed
432 frequency facilitation, differentiating it from paired pulse facilitation that relies on a residual
433 calcium-dependent transient increase in the p_v of releasable vesicles (Neher, 2024).
434 Assuming an increase in TS occupancy, to attain a two-fold increase in EPSC (Fig. 1), the
435 baseline occupancy of the docking sites by TS vesicles should be low, as estimated from the
436 V-M plot (c.a. 30% in Fig. 3). However, it is unclear whether the remaining docking sites that
437 are not occupied by TS vesicles are truly vacant or are occupied by reluctant LS vesicles that
438 are not released by the AP or AP trains. TS vesicles can be supplied by the transformation of
439 LS to TS vesicles, both of which reside at the same docking site (LS/TS model; reviewed in
440 Neher, 2024). Alternatively, TS vesicles can be supplied from a distinct replacement pool
441 (RS/DS model; reviewed in Silva et al., 2021). Further studies, including ultrastructural
442 analyses of active zones, are required to address this issue.

443 Given the crucial role of Syt7 in facilitation (Fig. 5), the facilitation mechanisms are closely
444 related to how Syt7 mediates synaptic facilitation. Based on the slow kinetics of Syt7, previous
445 computational modeling studies have proposed that Syt7 may mediate short-term facilitation
446 through an activity-dependent increase in p_v (Turecek et al., 2016; Jackman and Regehr, 2017;
447 Turecek et al., 2017; Norman et al., 2023). The present study, however, found that both
448 facilitation and augmentation were mediated by overfilling of the release sites (Figs. 2–3).
449 Moreover, Syt7-KD synapses displayed slower recovery of TS vesicles (Fig. 7). These results
450 suggest that Syt7 is essential for activity-dependent overfilling of docking sites with TS vesicles.
451 Whereas the baseline EPSC was not altered (Fig. S3), and complementary changes in the
452 number of docking sites and their baseline occupancy were observed in Syt7 KD synapses (Fig.
453 6). These results raise a possibility that Syt7 may play a role in providing additional vacant
454 docking sites that can be overfilled during facilitation. It remains to be elucidated whether the
455 decrease in the number of docking sites at Syt7 KD synapses is related to the subcellular
456 localization of Syt7 to the plasma membrane of the active zone (Sugita et al., 2001; Vevea et
457 al., 2021).
458

459 *STP model in light of known Ca^{2+} binding kinetics of Syt7*

460 Syt7 acts as an upstream Ca^{2+} sensor that facilitates activity-dependent replenishment (Liu et
461 al., 2014; Bacaj et al., 2015; Chen et al., 2017; Tawfik et al., 2021). The present study shows
462 that EPSCs are mediated by TS vesicles both at rest and during activity-dependent facilitation.
463 Releasable vesicles are homogeneous, and Syt7-dependent overfilling is responsible for the

464 activity-dependent enhancement of EPSCs. Thus, we tested whether slowly developing
465 facilitation could be replicated within the framework of a simple refilling model based on the
466 known Ca^{2+} binding kinetics of Syt7 (Brandt et al., 2012). To this end, we made following
467 assumptions: (1) a Ca^{2+}-dependent increase in the forward refilling rate (k_1) requires a full
468 Ca^{2+}-bound form of Syt7, to which multiple Ca^{2+} ions can bind (two or three Ca^{2+} ions on each
469 C2A and/or C2B domain) (Brandt et al., 2012; Chon et al., 2015; Voleti et al., 2017); (2)
470 sequential Ca^{2+} binding steps are synergistic through a cooperativity factor, *b*; (3) Syt7 senses
471 AP-induced local [Ca^{2+}] similar to that estimated at the calyx of Held (a Gaussian function with
472 a full width at half maximum value of 0.2 ms and a peak of 40 µM) (Wang et al., 2008); and
473 (4) residual [Ca^{2+}] follows a mono-exponential function with an amplitude of 1 µM and decay
474 time constant of 50 ms (Jackson and Redman, 2003).
475 Under these assumptions and the framework of the simple refilling model, slow and delayed
476 facilitation could be replicated by modeling k_1 as $k_1 = k_{1,b} + K_{1,max} \times$ [Syt7: n Ca^{2+}], where [Syt7:
477 n Ca^{2+}] represents the fraction of fully Ca^{2+}-bound Syt7 (Fig. 9A-C). Syt7 was slowly activated
478 over the course of the stimulus train, suggesting that the cooperative binding of multiple Ca^{2+}
479 ions progressively increased the putative active form of Syt7 because of its slow membrane
480 binding/unbinding kinetics. Nevertheless, the late phase of facilitation at high frequencies
481 was predicted to be higher in the simulation than in the experiment. As expected, based on
482 the notion that sustained release during HFS is limited by site clearance in the active zone (Fig.
483 4C), the model/data discrepancy became more pronounced at higher frequencies.
484 Incorporating endocytic terms into the model may mitigate late-phase discrepancies.

485 Moreover, removal of the catalytic function of Syt7 in the model effectively accounted for the
486 complete loss of facilitation observed in Syt7 KD (Fig. 9D).
487

488 *Possible mechanisms underlying the depression-facilitation sequence*

489 Cooperative binding of multiple Ca^{2+} ions to Syt7 predicts delayed activation and a progressive
490 increase in vesicle refilling during train stimulations, resulting in delayed facilitation.
491 Combining this with a high p_v could replicate not only the slow facilitation at 5 Hz, but also
492 the unique depression-facilitation sequence observed at 40 Hz (Fig. 9). As simulated by Pulido
493 and Marty (2018), delayed facilitation can be reproduced by a high p_v in combination with a
494 low baseline occupancy of replacement sites and subsequent Ca^{2+}-dependent refilling.
495 However, whether this model is also able to replicate slow facilitation at low frequencies
496 remains to be tested. An alternative, but not exclusive, possibility for delayed facilitation is
497 that the presynaptic global Ca^{2+} itself may undergo a slow buildup during a train due to the
498 saturation of endogenous Ca^{2+}-binding proteins.
499

500 *Facilitation requires not only Syt7, but also activation of PLC-DAG signaling*

501 To gain insight into the specific molecular mechanisms underlying the vesicle-loading
502 processes, we examined the effects of pharmacological inhibitors targeting PLC and DAG (Fig.
503 4). Both a PLC inhibitor and a DAG analog reduced facilitation and augmentation. This
504 suggests that the progressive overfilling of docking sites with TS vesicles is supported by the
505 PLC-DAG signaling pathway and probably downstream Munc13 (Rhee et al., 2002; Lou et al.,

506 2008). Phorbol esters have been recently shown to increase the TS fraction of docked vesicles
507 by enhancing vesicle priming without affecting Ca^{2+} transients or p_v (Taschenberger et al.,
508 2016; Aldahabi et al., 2022; Papantoniou et al., 2023; Aldahabi et al., 2024). In line with these
509 findings, signaling involving PLC and DAG may support Ca^{2+}-dependent overfilling of TS
510 vesicles by enhancing molecular priming processes.
511

512 *Roles of facilitation and augmentation in working memory and related tasks*

513 Previous theoretical studies have proposed that working memory in a recurrent network can
514 be maintained in the form of augmentation at synapses (Mongillo et al., 2008) and/or
515 persistent activity of neurons in a memory ensemble. This is supported by the facilitation of
516 recurrent excitatory synapses or disparity in STP between excitatory and inhibitory synapses.
517 However, whether these short-term enhancements in synaptic efficacy contribute to working
518 memory-related behaviors has not been examined. tFC is a temporal associative learning task
519 requiring temporary retention of CS information during a trace period. The mPFC and
520 hippocampus are crucial for tFC, and tFC is interfered with by a load of working memory and
521 attention distraction, implying that the tFC shares the same neural substrate with other
522 working memory tasks. In this study, tFC in WT and Syt7 KD animals revealed that Syt7
523 deficiency in the L2/3 pyramidal neurons of the mPFC impaired the acquisition of trace fear
524 memory and reduced c-Fos expression associated with tFC training (Fig. 8). Given that
525 synaptic enhancements in prelimbic L2/3 recurrent excitatory synapses can be attributed to

526 an increase in p_{occ}, these behavioral results suggest that presynaptic high Ca^{2+} transients are

527 temporally memorized in the presynaptic terminal as an increase in TS occupancy.

528

529 *Conclusions*

530 Progressive overfilling of synaptic vesicles with a high fusion probability supports the

531 facilitation and augmentation of recurrent excitatory synapses within the L2/3 network of the

532 mPFC and is essential for temporal associative learning.

533

534

535 ## Materials and Methods

536 *Animals/Subjects*

537 All experiments were carried out on Sprague-Dawley rats of either sex at p28-43. Rats were
538 maintained in temperature-controlled rooms on a constant 12 h light/12 h dark cycle and
539 were given access to water and food ad libitum. All animal procedures were approved and
540 performed in accordance with the Institutional Animal Care and Use Committee at Seoul
541 National University (SNU200522-1).

542

543 *In utero electroporation (IUE)*

544 Pregnant Sprague Dawley rats on embryonic day (E) 17.5 were deeply anesthetized with 5%
545 (v/v) isoflurane for the duration of surgery. The uterine horns were exposed by laparotomy
546 and wet with warm sterile phosphate-buffered saline (PBS). The plasmids (0.5-2 μg/μl)
547 together with the 0.01% fast green dye were injected into either the left or the right lateral
548 ventricle or bilateral ventricles of embryos through a thin glass capillary (Narishige PC-10).
549 The embryo's head was carefully held between the forceps-shaped electrodes of 10 mm
550 diameter (CUY65010; NEPAGENE, Japan). Electroporation pulses (50 V for 50 ms) were
551 delivered five times at intervals of 150 ms using a square-wave generator (ECM830; BEX,
552 United States). The uterine horns were placed back into the abdominal cavity and abdominal
553 muscles and skin were sutured. After the surgery, the animals were recovered under the
554 infrared lamp. For knockdown experiments in slice electrophysiology, the shRNA constructs
555 were co-electroporated with the pCAG-oChIEF-tdTomato, because of the consistent co-

556 expression of the two constructs in a significant proportion of the transfected cells in vivo
557 (Bony et al., 2013). Pups with robust fluorescence signals in the prefrontal cortex of both
558 hemispheres were used for behavior experiments.
559

560 *Preparation of vector constructs*

561 For an optic stimulation, pCAG-oChIEF-tdTomato was transfected by IUE. Short hairpin RNA
562 (shRNA) against Syt7 sequence (GATCTACCTGTCCTGGAAGAG) was expressed under the
563 control of an U6 promoter of pAAV-U6-GFP vector (Cell Biolabs, #VPK-413). This shRNA was
564 shown to effectively knockdown Syt7 in cell cultures and in vivo by previous reports from
565 more than one research group (Bacaj et al., 2013; Li et al., 2017). Scrambled control sequence
566 (TCGCATAGCGTATGCCGTT) was designed by shuffling the recognition region sequences and
567 a BLAST analysis confirmed that the control shRNA sequence had no target gene. For rescue
568 experiments, the cDNA for rat Syt7 (NM_021659) rendered resistant to the shRNA were
569 inserted in the KD vector and their expression was driven by the CAG promoter; the vector
570 also contained a self-cleaving P2A peptide sequence followed by EGFP, which ensures
571 visualization of transfected cells. All the constructs above were verified by DNA sequencing.
572 Plasmid DNA was purified and concentrated under endotoxin free conditions (Qiagen
573 EndoFree Maxi Kit).
574

575 *Slice preparation*

576 Acute brain slices were prepared by using a VT1200S Vibratome (Leica Microsystems) after
577 isoflurane anesthesia and decapitation. Coronal sections of the mPFC (300 µm in thickness)
578 were cut in ice-cold artificial cerebrospinal fluid (aCSF) composed of (in mM) 125 NaCl, 3.2
579 KCl, 25 $NaHCO_3$, 1.25 NaH_2PO_4, 20 D-glucose, 2 NaPyr, 1 $MgCl_2$, and 1.3 $CaCl_2$ (Yoon et al.,
580 2020), bubbled with 95% O_2 and CO_2 (pH = 7.3; 310 mOsm). Slices were allowed to recover
581 for a minimum of 30 minutes at 36 °C, and subsequently maintained at room temperature
582 until recording. Composition of aCSF was identical throughout the preparation, incubation,
583 and recording periods unless otherwise stated. For the recordings, the mPFC slices were
584 continuously perfused with oxygenated aCSF at a flow rate of 1.5 ml/min, and the
585 temperature was maintained at 31–32 °C using an in-line temperature controller (Warner
586 Instruments).

587

588 *Electrophysiology*

589 Whole-cell patch-clamp recordings were performed from pyramidal cells and fast-spiking
590 interneurons in layer 2/3 of the prelimbic mPFC. Neuronal subtypes were initially selected
591 based on morphology under visual guidance by using an upright microscope equipped with
592 infrared differential interference contrast (IR-DIC) optics (BX51WI, Olympus), and were
593 further identified by their electrophysiological properties (see Supplementary Fig. 1; van
594 Aerde and Feldmeyer, 2015; Tremblay et al., 2016). To analyze these intrinsic properties in
595 current-clamp experiments, we measured the following parameters: (1) resting membrane

596 potential (RMP), (2) input resistance (R_{in}), (3) sag ratio, and (4) the F-I curve, which plots firing
597 frequencies (F) against the amplitude of injected currents (I). Both cell types exhibited a low
598 sag ratio below 0.1, consistent with findings from other studies (van Aerde and Feldmeyer,
599 2015; Yoon et al., 2020). PCs and FSINs were easily distinguished by their unique firing
600 frequency, Rin, spike adaptation, RMP and morphological characteristics including the shape
601 of soma and the thickness of apical dendrites. For experiments involving oChIEF-expressing
602 neurons in WT or Syt7 KD rats, whole-cell recordings were performed from the fluorescently
603 labeled pyramidal neurons in layer 2/3 of the prelimbic cortex using suitable filter sets. Patch
604 pipettes (tip resistance of 2–3 MΩ) were pulled from borosilicate glass and filled with (in mM)
605 130 K-gluconate, 8 KCl, 10 HEPES, 0.2 EGTA, 20 Na_2Pcr, 0.3 Na_2GTP, 4 MgATP. Intracellular
606 solutions were adjusted to pH 7.25 and 300–310 mOsm. Neurons were voltage clamped at
607 −78 mV and series resistance (Rs) were continuously monitored during the EPSCs recordings.
608 Experiments were discarded before analysis if the Rs changed by 20% or larger deviation of
609 baseline value. Measurements were not corrected for Rs compensation, bridge balance, or
610 liquid junction potential. Electrophysiological data were low-pass-filtered at 1 kHz (Bessel)
611 and acquired at 20 kHz using a Multiclamp 700B amplifier paired with Digidata 1440A digitizer
612 and Clampex 10.2 software (Molecular Devices).
613

614 *Synaptic stimulation*

615 IUE resulted in sparse expression of channelrhodopsin (10-20%) (Fig. 1A). Exploiting the
616 sparse expression, we employed a minimal optical stimulation method to activate a single or
617 very few excitatory synapses in layer 2/3. The optic minimal stimulation was performed by

618 our published protocol with minor modifications (Yoon et al., 2020). This approach aimed to
619 minimize the risk of synaptic contamination, which could arise from engaging extra terminals
620 that were initially inactive (depolarized below threshold) but became active by temporal
621 summation during high-frequency trains. It also helped prevent the buildup of depolarization
622 at the synaptic terminals, which might influence the probability of release, as noted by
623 (Jackman et al., 2014). To achieve this, we employed a collimated digital micromirror device
624 (DMD)-coupled LED (Polygon400; Mightex Systems) to confine 470 nm blue light to a small
625 area with a radius of approximately 3–8 µm (typically 3–4 µm), as measured at the focal plane
626 of a 60× water immersion objective [numerical aperture (NA) = 1.0; LUMPlanFL, Olympus] (Fig.
627 S3A). To find the minimal stimulation area, the radius of illumination area was increased from
628 2 µm by 50% at each step (Fig. S3A), and selected the smallest illumination area that elicited
629 EPSCs. Setting the duration of illumination between 3 and 5 ms (typically 5 ms),
630 photostimulation onto oChIEF-expressing cells reliably induced action potentials (APs) during
631 600-pulse trains (see Fig. S2).
632 STP at various stimulus frequencies (5, 10, 20, and 40 Hz) was examined using 20-pulse trains.
633 Trials of train stimulation were repeated with a prolonged interval of 30 s to avoid change in
634 baseline properties. We observed no systematic changes in the amplitudes of the first EPSC
635 of each train, nor did we find significant differences in the paired-pulse ratio (PPR) across
636 stimulation trials in the same cell. For each stimulus frequency, approximately ten to twenty
637 consecutive traces were collected and then averaged across trials to yield a mean EPSC trace.
638 For recovery experiments, two consecutive trains of 3 or 30 stimuli at 40 Hz, with varying time
639 intervals (0.1-10 s), were applied every 10 s or 60 s, respectively, at both excitatory synapses.

640 For 600-stimulus trains at 10Hz, the trial was delivered only once for each cell to avoid
641 possible after-effects caused by prolonged synaptic stimulation (Hirsch and Crepel, 1990).
642 Prior to the stimulus trains, the EPSCs were normalized to the mean amplitude of the baseline.
643 For the baseline measurements, paired pulses with various ISIs (20-200 ms) were delivered
644 every 3 s (1/3 Hz) at least 20 times.
645 For all recordings, picrotoxin (PTX, 10 µM) was included in the recording solution to isolate
646 glutamatergic responses. mPFC PC terminals were entirely glutamatergic as the application
647 of 6-cyano-7-nitroquinoxaline-2,3-dione (CNQX, 20 µM), an AMPA receptor antagonist,
648 completely abolished the monosynaptic events evoked by photostimulation. A low
649 concentration of PTX was employed to minimize the relieving effects on spike suppression
650 caused by blockade of GABAa receptors. We confirmed that no synaptic response was elicited
651 by electrical stimulation in the presence of both 10 µM PTX and 20 µM CNQX.
652 In Fig. S4A, 1 µM TTX (1 mM stock solution) and 0.1 mM 4-AP (500 mM stock solution) were
653 added to the bath solution to block action potentials and restore presynaptic glutamate
654 release, respectively (Fig. S4A). In Fig. S5A, 50 µM of cyclothiazide, a positive allosteric
655 modulator of the AMPA receptors, was included to minimize rapid desensitization of the
656 postsynaptic receptors. In Fig. S5B, 0.5 mM kynurenate was added to bath solution to prevent
657 possible saturation of AMPA receptors, especially during maximal synaptic facilitation. For
658 pharmacological manipulations of synaptic vesicle dynamics (Fig. 3), drugs related to vesicle
659 supply including U73122, OAG, LatB, EGTA-AM, and dynasore at indicated concentrations
660 were added to the recording solution during baseline measurements or PTA/recovery
661 experiments (IBI = 0.5 s). Chemicals were from Sigma-Aldrich, Merck, or Tocris.

662

663 *Measurements of quantal size*

664 Experiments for measuring asynchronous release were performed as previously described
665 (Yoon et al., 2020). In brief, we replaced extracellular Ca^{2+} entirely with 2 mM Sr^{2+} to induce
666 asynchronous release. A single stimulus was delivered at 3-second intervals over 100
667 repetitions, and asynchronous release events were detected during a 100-ms window starting
668 25 ms after stimulus onset for each trial. The same procedure was also executed under sham
669 conditions (0% light intensity) to serve as a control, thus mitigating contamination from
670 nonspecific spontaneous events and potential errors associated with in the detection
671 algorithm. q was determined as the mean value from the first Gaussian function after fitting
672 the EPSC distribution with either a single or double Gaussian function (Fig. S8).

673

674 *Calculation of probability for double failure*

675 The failure rate at the 1st pulse when initial RRP size (n_1) = *i* can be calculated as: $P(F_1 \mid n_1=i)$
676 $= (1 - p_v)^i$. The probability that initial RRP size is *i* was calculated as: $P(n_1=i) = C(N, i) * p_{occ}^i *$
677 $(1-p_{occ})^{(N-i)}$, where p_{occ} = mean release site occupancy, and N = total number of release sites.
678 Under the conditions of no vesicle release at the 1st pulse (F_1) and $n_1 = i$, the probability for
679 the second failure is

680 $$P(F_2 \mid n_1=i, F_1) = \Sigma_{n2=0..N} P(n_2 \mid n_1=i, F_1)\,(1 - p_v)^{n2} .$$

681 , where n_2 = number of vesicles just before the 2nd pulse. When forward and backward rate
682 constants are k_1 and b_1, respectively, $P(n_2 \mid n_1=i, F1)$ is calculated as follows:

683 $$\text{If } n_2>i,\ P(n_2 \mid n_1=i, F1) = C(N-i, n_2-i)\,[1-\exp(-k_1\,\Delta t)]^{(n2-i)}.$$

684 $$\text{If } n_2<i,\ P(n_2 \mid n_1=i, F1) = C(i, i-n_2)\,[1-\exp(-b_1\,\Delta t)]^{(i-n2)}.$$

685 $$\text{If } n_2=i,\ P(n_2 \mid n_1=i, F1) = \exp[-i\,k1\,\Delta t]\,\exp[-i\,b_1\,\Delta t].$$

686 , where Δt = ISI. By the Bayes rule,

687 $$P(F_1, F_2, n_1=i) = P(F_2 \mid n_1=i, F_1)\,P(F_1 \mid n_1=i)\,P(n_1=i).$$

688 Thus, the probability for two consecutive failures can be calculated as:

689 $$P(F_1, F_2) = \Sigma_{i=0..N}\,P(F_2 \mid n_1 = i, F_1)\,P(F_1 \mid n_1=i)\,P(n_1=i).$$

690 $P(F_1)$ and N are observed values. The k_1 and p_v were set free variables. Other parameters were

691 set according to following relationships: $P(F_1) = (1-p_r)^N$, $p_r = p_v\,p_{occ}$, and $p_{occ} = k_1 / (k_1 + b_1)$.

692

693 *Behavioral tests*

694 **Trace fear conditioning**: For trace fear conditioning (tFC) (Gilmartin et al., 2013), individual

695 rats were placed in the training chamber (30.5 x 25.4 x 30.5 cm; Coulbourn Instruments)

696 consisting of metal grid floor connected to an electrical stimulator (H10-11R-TC-SF, Coulbourn

697 Instruments) for delivery of a footshock. After a 5 min habituation period, rats received five

698 pairings of a 20 s tone conditioned stimulus (CS, 2.5 kHz, 75 dB), followed by empty 20s trace

699 period and a unconditioned stimulus (US; 1 s, 0.7 mA footshock) with a pseudorandom inter-

700 trial interval (ITI) of 240 ± 20 s. During this training session, rats learned to associate the

701 auditory CS with the shock US. The next day, the rats were tested for memory of CS-US trace

702 association (called tone test). The acquisition of fear learning, often indicated by the extent

703 of freezing to the CS, was assessed in a novel chamber (a white hexagonal enclosure) in a

704 dimly lit room. During this tone (or retrieval) test, rats were first allowed to explore the new

705 context for 5 min (habituation), followed by twelve 20 s CS presentations with a variable ITI
706 of 120 ± 20 s. This entire session was repeated on the next day for assessment of extinction
707 learning. Identities of the chambers were also determined with the presence of distinct odors;
708 the training and testing chambers were cleaned with 70% ethanol and 1% acetic acid
709 respectively before and after each session. For all experimental sessions, the activity of
710 animals in the chambers was recorded at 30 frames per second using the EthoVision XT
711 (Noldus Information Technology, Wageningen, Netherlands), and stored as a video file. The
712 freezing behavior, defined as behavioral immobility other than respiratory movement, was
713 assessed using an open-source video analysis pipeline ezTrack (Pennington et al., 2019). The
714 percentage of freezing was calculated as a total duration of freezing divided by the total
715 duration of observation.
716 **Elevated Plus Maze**: Elevated plus maze (EPM) test was performed using a plus-shaped
717 apparatus elevated 60 cm above the ground. The maze consisted of two open arms (50 x 10
718 x 0.5 cm (H)), two closed arms (50 x 10 x 40 cm (H)) and a center area (10 x 10 cm). Rats were
719 individually placed on the center area, facing an open arm, and the path of the animal was
720 recorded with a video camera for 5 min. We analyzed the total distance traveled for 5 min
721 and time spent in each arm. Animals were tracked offline using the open-source tracking
722 system ezTrack (Pennington et al., 2019).
723 **Open field test**: Open field exploration test (OFT) was performed in an open field apparatus
724 in a dimly lit room. The open field consisted of a white plastic board (1.20 m in diameter)
725 surrounded by white plastic walls (50 cm in height). Individual rats were placed in a center
726 zone (0.6 m in diameter), and allowed to freely explore the apparatus for 10 min. Time spent

727 in the center zone and total distance traveled were analyzed for initial 5 min. Animals were
728 tracked offline using the open-source tracking system ezTrack (Pennington et al., 2019).
729

730 *Histology and immunohistochemistry*

731 At the end of the behavioral experiments, rats were anesthetized using isoflurane inhalation
732 and transcardially perfused with PBS followed by 4% paraformaldehyde (PFA, T&I, Korea).
733 Brains were extracted and post-fixed in 4% PFA solution for 24 h. Perfused brains were sliced
734 at 100 μm for estimation of GFP expression or 50 μm for immunohistochemistry. For analysis
735 of c-Fos expression, rats were returned to their home cages immediately after the training
736 session and perfused approximately 90 minutes later (Arime and Akiyama, 2017). Brains were
737 then cryopreserved, frozen, and sectioned coronally. Immunofluorescence staining was
738 conducted on free-floating slices using a rabbit monoclonal anti c-fos (1:1000, Cell Signaling
739 Technology, cat# 2250s) and mouse monoclonal anti-GAD67 (1:500, Millipore, cat# mab5406).
740 Fluorescent secondary antibodies included Cy5-conjugated goat anti-rabbit IgG (1:1000,
741 Abcam, cat# ab97077) and Cy3-conjugated goat anti-mouse IgG (1:1000, Abcam, cat#
742 ab97035). Brain slices were permeabilized and blocked with PBS containing 0.5% Triton X-100
743 and 5% normal goat serum (NGS) for 1h at room temperature. Slices were incubated
744 overnight at 4 °C with primary antibodies, followed by 4 h incubation with secondary
745 antibodies at room temperature. Slices were then mounted with Antifading Mounting
746 medium (Abcam, cat# ab104139). Confocal images were acquired using a Leica TCS SP8
747 microscope set to the same laser intensity and acquisition parameters to compare the
748 immunosignals in sections from Scr and Syt7 KD groups. For cell counting and colocalization,

749 fluorescent protein-positive cells were automatically quantified with spot-detection
750 algorithms in Imaris 9.5 (Oxford instruments).
751

752 *Data analysis*

753 Data were analyzed and presented using ClampFit (Molecular Devices), Igor Pro
754 (Wavemetrics), MATLAB (Mathworks), and Prism (GraphPad). Data points and error bars
755 represent the mean ± standard error of the mean. All statistical analyses were conducted
756 using two-tailed comparisons. Sample sizes and statistical tests for each group are detailed in
757 the figure legends.
758

759 *Numerical integration of the simple refilling model*

760 This model posits reversible docking of vesicles at finite release sites (N_{max}) with forward (k_1)
761 and reverse rate constants (b_1) (Hosoi et al., 2007; Neher and Sakaba, 2008).

$$\underset{b_1}{\overset{k_1}{\rightleftarrows}} n \xrightarrow{p_v}$$

762

763 According to this scheme, $dn/dt = k1\ u - b1\ n - p_v\ n\ \delta(t - t_{AP})$, where u is the number of
764 unoccupied sites (= $N_{max} - n$); t_{AP} is the timing of AP firing; and δ is the Dirac delta function.
765 The p_v was assumed to be unity (Fig. S8). The sum of basal k_1 (= $k_{1,b}$) and b_1 was be estimated
766 as 23/s from the dependence PPR on ISIs (Fig. S8Ab). From the baseline occupancy of 0.3 and
767 $p_{occ} = k_1 / (k_1 + b_1)$, we could estimate baseline k_1 ($k_{1,b}$) and b1 as 6.9/s, and 16.1/s, respectively.

768 Ca^{2+}- and Syt7-dependent increase of k_1 was modeled as $k_1 = k_{1,b} + K_{1,max}$ [Syt7: n Ca^{2+}], where
769 [Syt7: n Ca^{2+}] represents the fraction of full Ca^{2+}-bound Syt7. For deterministic simulations,
770 we time-integrated a set of differential equations for each model using Euler methods with a
771 time step of 1 ms. All calculations were performed on the platform of Matlab (R2022b,
772 Mathworks, USA).
773

774 ## Acknowledgements

775 We thank Dr. E. Neher and Dr. A. Marty for critical reading of this manuscript and
776 invaluable comments.
777

778 ## Author contributions

779 All experiments were carried out at cell physiology lab under Y.K and S.H.L's supervision.
780 Conception or design of the work: J.S. and S.H.L. Acquisition, analysis or interpretation of data
781 for the work: J.S, Y.K. and L.S.H. Drafting the work or revising it critically for important
782 intellectual content: J.S., S.Y.L, Y.K. and L.S.H.
783

784 ## Funding

785 This study was supported by grants from the National Research Foundation of Korea (RS-
786 2024-333669 to S-H. Lee; 2021R1I1A1A01059646 to Y. Kim), and Seoul National University
787 Hospital (2024).
788
789

790 ## References

791 Aldahabi M, Neher E, Nusser Z (2024) Different states of synaptic vesicle priming explain
792 target cell type-dependent differences in neurotransmitter release. Proc Natl Acad Sci
793 U S A 121:e2322550121.
794 Aldahabi M, Balint F, Holderith N, Lorincz A, Reva M, Nusser Z (2022) Different priming states
795 of synaptic vesicles underlie distinct release probabilities at hippocampal excitatory
796 synapses. Neuron 110:4144-4161 e4147.
797 Arime Y, Akiyama K (2017) Abnormal neural activation patterns underlying working memory
798 impairment in chronic phencyclidine-treated mice. PLoS One 12:e0189287.
799 Bacaj T, Wu D, Burre J, Malenka RC, Liu X, Sudhof TC (2015) Synaptotagmin-1 and -7 Are
800 Redundantly Essential for Maintaining the Capacity of the Readily-Releasable Pool of
801 Synaptic Vesicles. PLoS Biol 13:e1002267.
802 Bacaj T, Wu D, Yang X, Morishita W, Zhou P, Xu W, Malenka RC, Sudhof TC (2013)
803 Synaptotagmin-1 and synaptotagmin-7 trigger synchronous and asynchronous phases
804 of neurotransmitter release. Neuron 80:947-959.
805 Baeg EH, Kim YB, Huh K, Mook-Jung I, Kim HT, Jung MW (2003) Dynamics of population code
806 for working memory in the prefrontal cortex. Neuron 40:177-188.
807 Bony G, Szczurkowska J, Tamagno I, Shelly M, Contestabile A, Cancedda L (2013) Non-
808 hyperpolarizing GABAB receptor activation regulates neuronal migration and neurite
809 growth and specification by cAMP/LKB1. Nat Commun 4:1800.
810 Brandt DS, Coffman MD, Falke JJ, Knight JD (2012) Hydrophobic contributions to the
811 membrane docking of synaptotagmin 7 C2A domain: mechanistic contrast between
812 isoforms 1 and 7. Biochemistry 51:7654-7664.
813 Chen C, Satterfield R, Young SM, Jr., Jonas P (2017) Triple Function of Synaptotagmin 7
814 Ensures Efficiency of High-Frequency Transmission at Central GABAergic Synapses.
815 Cell Rep 21:2082-2089.
816 Chon NL, Osterberg JR, Henderson J, Khan HM, Reuter N, Knight JD, Lin H (2015) Membrane
817 Docking of the Synaptotagmin 7 C2A Domain: Computation Reveals Interplay between
818 Electrostatic and Hydrophobic Contributions. Biochemistry 54:5696-5711.
819 Dittman JS, Kreitzer AC, Regehr WG (2000) Interplay between facilitation, depression, and
820 residual calcium at three presynaptic terminals. J Neurosci 20:1374-1385.
821 Fields RD, Eshete F, Stevens B, Itoh K (1997) Action potential-dependent regulation of gene
822 expression: temporal specificity in ca2+, cAMP-responsive element binding proteins,
823 and mitogen-activated protein kinase signaling. J Neurosci 17:7252-7266.
824 Fujisawa S, Amarasingham A, Harrison MT, Buzsaki G (2008) Behavior-dependent short-term
825 assembly dynamics in the medial prefrontal cortex. Nat Neurosci 11:823-833.
826 Gilmartin MR, Miyawaki H, Helmstetter FJ, Diba K (2013) Prefrontal activity links
827 nonoverlapping events in memory. J Neurosci 33:10910-10914.
828 Guzowski JF, Timlin JA, Roysam B, McNaughton BL, Worley PF, Barnes CA (2005) Mapping
829 behaviorally relevant neural circuits with immediate-early gene expression. Curr Opin
830 Neurobiol 15:599-606.

831 Hallermann S, Silver RA (2013) Sustaining rapid vesicular release at active zones: potential
832 roles for vesicle tethering. Trends Neurosci 36:185-194.
833 Hansel D, Mato G (2013) Short-term plasticity explains irregular persistent activity in working
834 memory tasks. J Neurosci 33:133-149.
835 Hass CA, Glickfeld LL (2016) High-fidelity optical excitation of cortico-cortical projections at
836 physiological frequencies. J Neurophysiol 116:2056-2066.
837 Haucke V, Neher E, Sigrist SJ (2011) Protein scaffolds in the coupling of synaptic exocytosis
838 and endocytosis. Nat Rev Neurosci 12:127-138.
839 Hempel CM, Hartman KH, Wang XJ, Turrigiano GG, Nelson SB (2000) Multiple forms of short-
840 term plasticity at excitatory synapses in rat medial prefrontal cortex. J Neurophysiol
841 83:3031-3041.
842 Hirsch JC, Crepel F (1990) Use-dependent changes in synaptic efficacy in rat prefrontal
843 neurons in vitro. J Physiol 427:31-49.
844 Holler S, Kostinger G, Martin KAC, Schuhknecht GFP, Stratford KJ (2021) Structure and
845 function of a neocortical synapse. Nature 591:111-116.
846 Holmgren C, Harkany T, Svennenfors B, Zilberter Y (2003) Pyramidal cell communication
847 within local networks in layer 2/3 of rat neocortex. J Physiol 551:139-153.
848 Hosoi N, Sakaba T, Neher E (2007) Quantitative analysis of calcium-dependent vesicle
849 recruitment and its functional role at the calyx of Held synapse. J Neurosci 27:14286-
850 14298.
851 Jackman SL, Regehr WG (2017) The Mechanisms and Functions of Synaptic Facilitation.
852 Neuron 94:447-464.
853 Jackman SL, Beneduce BM, Drew IR, Regehr WG (2014) Achieving high-frequency optical
854 control of synaptic transmission. J Neurosci 34:7704-7714.
855 Jackman SL, Turecek J, Belinsky JE, Regehr WG (2016) The calcium sensor synaptotagmin 7 is
856 required for synaptic facilitation. Nature 529:88-91.
857 Jackson MB, Redman SJ (2003) Calcium dynamics, buffering, and buffer saturation in the
858 boutons of dentate granule-cell axons in the hilus. J Neurosci 23:1612-1621.
859 Kobbersmed JRL, Grasskamp AT, Jusyte M, Böhme MA, Ditlevsen S, Sørensen JB, Walter AM
860 (2020) Rapid regulation of vesicle priming explains synaptic facilitation despite
861 heterogeneous vesicle:Ca2+ channel distances. eLife 9:e51032.
862 Kusick GF, Chin M, Raychaudhuri S, Lippmann K, Adula KP, Hujber EJ, Vu T, Davis MW,
863 Jorgensen EM, Watanabe S (2020) Synaptic vesicles transiently dock to refill release
864 sites. Nat Neurosci 23:1329-1338.
865 Lee HR, Choi SH, Lee SH (2024) Differential involvement of mitochondria in post-tetanic
866 potentiation at intracortical excitatory synapses of the medial prefrontal cortex. Cereb
867 Cortex 34.
868 Lee JS, Ho WK, Lee SH (2010) Post-tetanic increase in the fast-releasing synaptic vesicle pool
869 at the expense of the slowly releasing pool. J Gen Physiol 136:259-272.
870 Lee JS, Ho WK, Lee SH (2012) Actin-dependent rapid recruitment of reluctant synaptic vesicles
871 into a fast-releasing vesicle pool. Proc Natl Acad Sci U S A 109:E765-774.
872 Li YC, Chanaday NL, Xu W, Kavalali ET (2017) Synaptotagmin-1- and Synaptotagmin-7-
873 Dependent Fusion Mechanisms Target Synaptic Vesicles to Kinetically Distinct
874 Endocytic Pathways. Neuron 93:616-631 e613.

875 Lin JY, Lin MZ, Steinbach P, Tsien RY (2009) Characterization of engineered channelrhodopsin
876 variants with improved properties and kinetics. Biophys J 96:1803-1814.
877 Lin KH, Taschenberger H, Neher E (2022) A sequential two-step priming scheme reproduces
878 diversity in synaptic strength and short-term plasticity. Proc Natl Acad Sci U S A
879 119:e2207987119.
880 Liu H, Bai H, Hui E, Yang L, Evans CS, Wang Z, Kwon SE, Chapman ER (2014) Synaptotagmin 7
881 functions as a Ca2+-sensor for synaptic vesicle replenishment. Elife 3:e01524.
882 Lou X, Korogod N, Brose N, Schneggenburger R (2008) Phorbol esters modulate spontaneous
883 and Ca2+-evoked transmitter release via acting on both Munc13 and protein kinase C.
884 J Neurosci 28:8257-8267.
885 Macia E, Ehrlich M, Massol R, Boucrot E, Brunner C, Kirchhausen T (2006) Dynasore, a cell-
886 permeable inhibitor of dynamin. Dev Cell 10:839-850.
887 Malagon G, Miki T, Tran V, Gomez LC, Marty A (2020) Incomplete vesicular docking limits
888 synaptic strength under high release probability conditions. Elife 9.
889 Markram H, Wang Y, Tsodyks M (1998) Differential signaling via the same axon of neocortical
890 pyramidal neurons. Proc Natl Acad Sci U S A 95:5323-5328.
891 Martinetti LE, Bonekamp KE, Autio DM, Kim HH, Crandall SR (2022) Short-Term Facilitation of
892 Long-Range Corticocortical Synapses Revealed by Selective Optical Stimulation. Cereb
893 Cortex 32:1932-1949.
894 Miki T, Malagon G, Pulido C, Llano I, Neher E, Marty A (2016) Actin- and Myosin-Dependent
895 Vesicle Loading of Presynaptic Docking Sites Prior to Exocytosis. Neuron 91:808-823.
896 Mongillo G, Barak O, Tsodyks M (2008) Synaptic theory of working memory. Science
897 319:1543-1546.
898 Mongillo G, Hansel D, van Vreeswijk C (2012) Bistability and spatiotemporal irregularity in
899 neuronal networks with nonlinear synaptic transmission. Phys Rev Lett 108:158101.
900 Neher E (2010) What is Rate-Limiting during Sustained Synaptic Activity: Vesicle Supply or the
901 Availability of Release Sites. Front Synaptic Neurosci 2:144.
902 Neher E (2024) Interpretation of presynaptic phenotypes of synaptic plasticity in terms of a
903 two-step priming process. J Gen Physiol 156.
904 Neher E, Sakaba T (2008) Multiple roles of calcium ions in the regulation of neurotransmitter
905 release. Neuron 59:861-872.
906 Neher E, Brose N (2018) Dynamically Primed Synaptic Vesicle States: Key to Understand
907 Synaptic Short-Term Plasticity. Neuron 100:1283-1291.
908 Norman CA, Krishnakumar SS, Timofeeva Y, Volynski KE (2023) The release of inhibition model
909 reproduces kinetics and plasticity of neurotransmitter release in central synapses.
910 Commun Biol 6:1091.
911 Otsuka T, Kawaguchi Y (2009) Cortical inhibitory cell types differentially form intralaminar and
912 interlaminar subnetworks with excitatory neurons. J Neurosci 29:10533-10540.
913 Ozdemir AT, Lagler M, Lagoun S, Malagon-Vina H, Lasztoczi B, Klausberger T (2020)
914 Unexpected Rule-Changes in a Working Memory Task Shape the Firing of Histologically
915 Identified Delay-Tuned Neurons in the Prefrontal Cortex. Cell Rep 30:1613-1626 e1614.
916 Pan B, Zucker RS (2009) A general model of synaptic transmission and short-term plasticity.
917 Neuron 62:539-554.

918 Papantoniou C, Laugks U, Betzin J, Capitanio C, Ferrero JJ, Sanchez-Prieto J, Schoch S, Brose
919 N, Baumeister W, Cooper BH, Imig C, Lucic V (2023) Munc13- and SNAP25-dependent
920 molecular bridges play a key role in synaptic vesicle priming. Sci Adv 9:eadf6222.
921 Pennington ZT, Dong Z, Feng Y, Vetere LM, Page-Harley L, Shuman T, Cai DJ (2019) ezTrack:
922 An open-source video analysis pipeline for the investigation of animal behavior. Sci
923 Rep 9:19979.
924 Pulido C, Marty A (2018) A two-step docking site model predicting different short-term
925 synaptic plasticity patterns. J Gen Physiol 150:1107-1124.
926 Reyes A, Sakmann B (1999) Developmental switch in the short-term modification of unitary
927 EPSPs evoked in layer 2/3 and layer 5 pyramidal neurons of rat neocortex. J Neurosci
928 19:3827-3835.
929 Rhee JS, Betz A, Pyott S, Reim K, Varoqueaux F, Augustin I, Hesse D, Sudhof TC, Takahashi M,
930 Rosenmund C, Brose N (2002) Beta phorbol ester- and diacylglycerol-induced
931 augmentation of transmitter release is mediated by Munc13s and not by PKCs. Cell
932 108:121-133.
933 Ritzau-Jost A, Jablonski L, Viotti J, Lipstein N, Eilers J, Hallermann S (2018) Apparent calcium
934 dependence of vesicle recruitment. J Physiol 596:4693-4707.
935 Ritzau-Jost A, Delvendahl I, Rings A, Byczkowicz N, Harada H, Shigemoto R, Hirrlinger J, Eilers
936 J, Hallermann S (2014) Ultrafast action potentials mediate kilohertz signaling at a
937 central synapse. Neuron 84:152-163.
938 Rozov A, Burnashev N, Sakmann B, Neher E (2001) Transmitter release modulation by
939 intracellular Ca2+ buffers in facilitating and depressing nerve terminals of pyramidal
940 cells in layer 2/3 of the rat neocortex indicates a target cell-specific difference in
941 presynaptic calcium dynamics. J Physiol 531:807-826.
942 Sakaba T, Neher E (2003) Involvement of actin polymerization in vesicle recruitment at the
943 calyx of Held synapse. J Neurosci 23:837-846.
944 Scheuss V, Schneggenburger R, Neher E (2002) Separation of presynaptic and postsynaptic
945 contributions to depression by covariance analysis of successive EPSCs at the calyx of
946 Held synapse. J Neurosci 22:728-739.
947 Silva M, Tran V, Marty A (2021) Calcium-dependent docking of synaptic vesicles. Trends
948 Neurosci 44:579-592.
949 Silva M, Tran V, Marty A (2024) A maximum of two readily releasable vesicles per docking site
950 at a cerebellar single active zone synapse. Elife 12.
951 Sugita S, Han W, Butz S, Liu X, Fernandez-Chacon R, Lao Y, Sudhof TC (2001) Synaptotagmin
952 VII as a plasma membrane Ca(2+) sensor in exocytosis. Neuron 30:459-473.
953 Taschenberger H, Woehler A, Neher E (2016) Superpriming of synaptic vesicles as a common
954 basis for intersynapse variability and modulation of synaptic strength. Proc Natl Acad
955 Sci U S A 113:E4548-4557.
956 Tawfik B, Martins JS, Houy S, Imig C, Pinheiro PS, Wojcik SM, Brose N, Cooper BH, Sorensen
957 JB (2021) Synaptotagmin-7 places dense-core vesicles at the cell membrane to
958 promote Munc13-2- and Ca(2+)-dependent priming. Elife 10.
959 Tran V, Silva M, Marty A (2023) Prioritized docking of synaptic vesicles provided by a rapid
960 recycling pathway. iScience 26:106366.

961 Tremblay R, Lee S, Rudy B (2016) GABAergic Interneurons in the Neocortex: From Cellular
962 Properties to Circuits. Neuron 91:260-292.
963 Turecek J, Jackman SL, Regehr WG (2016) Synaptic Specializations Support Frequency-
964 Independent Purkinje Cell Output from the Cerebellar Cortex. Cell Rep 17:3256-3268.
965 Turecek J, Jackman SL, Regehr WG (2017) Synaptotagmin 7 confers frequency invariance onto
966 specialized depressing synapses. Nature 551:503-506.
967 Valera AM, Doussau F, Poulain B, Barbour B, Isope P (2012) Adaptation of granule cell to
968 Purkinje cell synapses to high-frequency transmission. J Neurosci 32:3267-3280.
969 van Aerde KI, Feldmeyer D (2015) Morphological and physiological characterization of
970 pyramidal neuron subtypes in rat medial prefrontal cortex. Cereb Cortex 25:788-805.
971 Vandael D, Borges-Merjane C, Zhang X, Jonas P (2020) Short-Term Plasticity at Hippocampal
972 Mossy Fiber Synapses Is Induced by Natural Activity Patterns and Associated with
973 Vesicle Pool Engram Formation. Neuron 107:509-521 e507.
974 Vevea JD, Kusick GF, Courtney KC, Chen E, Watanabe S, Chapman ER (2021) Synaptotagmin 7
975 is targeted to the axonal plasma membrane through gamma-secretase processing to
976 promote synaptic vesicle docking in mouse hippocampal neurons. Elife 10.
977 Voleti R, Tomchick DR, Sudhof TC, Rizo J (2017) Exceptionally tight membrane-binding may
978 explain the key role of the synaptotagmin-7 C(2)A domain in asynchronous
979 neurotransmitter release. Proc Natl Acad Sci U S A 114:E8518-E8527.
980 Wang LY, Neher E, Taschenberger H (2008) Synaptic vesicles in mature calyx of Held synapses
981 sense higher nanodomain calcium concentrations during action potential-evoked
982 glutamate release. J Neurosci 28:14450-14458.
983 Wu LG, Chan CY (2022) Multiple Roles of Actin in Exo- and Endocytosis. Front Synaptic
984 Neurosci 14:841704.
985 Yau JO, McNally GP (2023) The Rescorla-Wagner model, prediction error, and fear learning.
986 Neurobiol Learn Mem 203:107799.
987 Yoon JY, Lee HR, Ho WK, Lee SH (2020) Disparities in Short-Term Depression Among Prefrontal
988 Cortex Synapses Sustain Persistent Activity in a Balanced Network. Cereb Cortex
989 30:113-134.
990 Zucker RS, Regehr WG (2002) Short-term synaptic plasticity. Annu Rev Physiol 64:355-405.
991

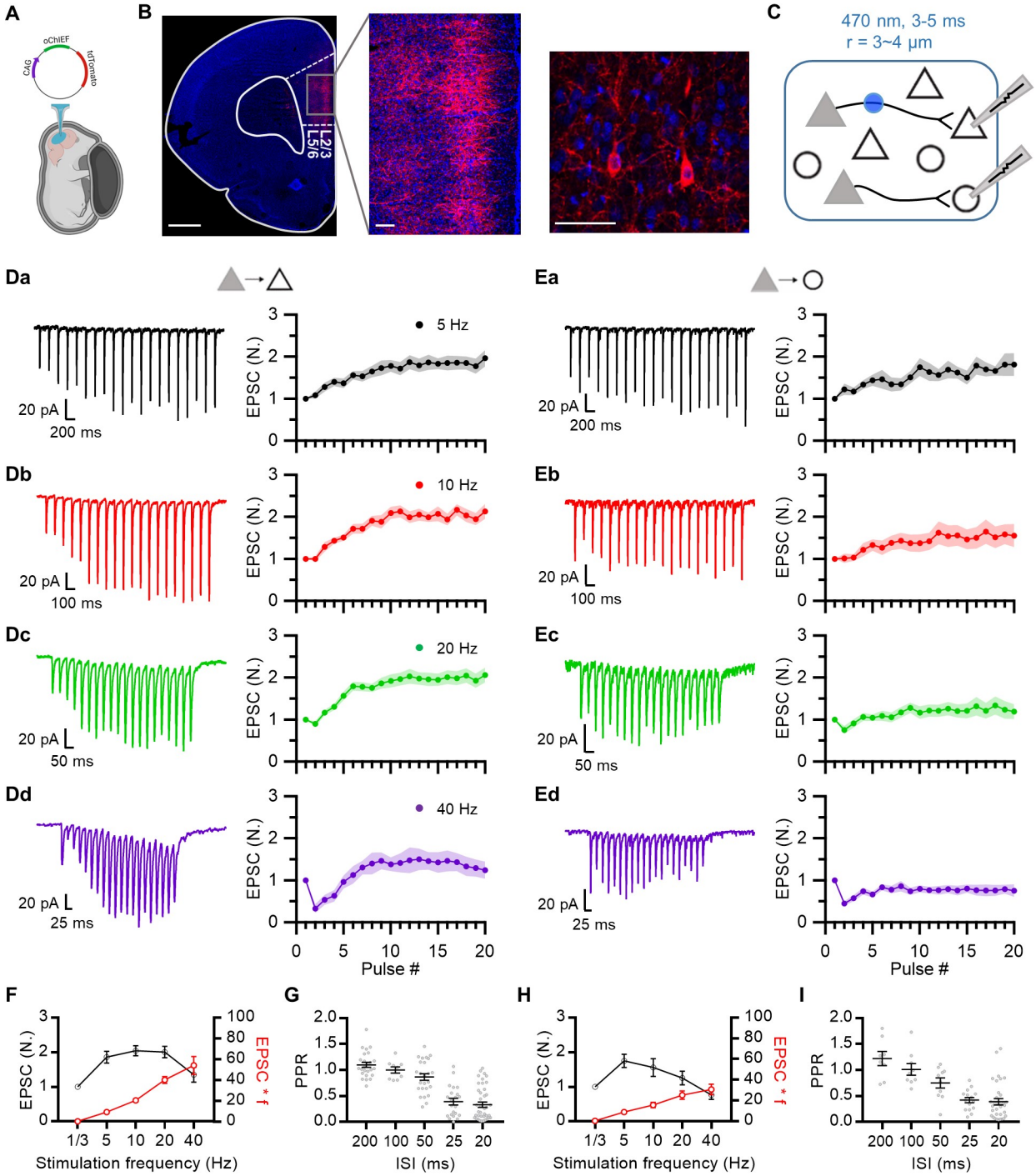

1 **Figure 1. Frequency-dependence of short-term synaptic plasticity at prelimbic L2/3**

2 **excitatory synapses.**

(**A**) In utero electroporation following injection of the plasmid (CAG-oChIEF-tdTomato) into the ventricle of an embryo (E17.5). (**B**) Representative images showing specific expression of oChIEF-tdTomato in L2/3 pyramidal cells after IUE. The red fluorescence of tdTomato clearly visualizes oChIEF-expressing cell bodies in L2/3 and axons in L5. Scale bar: 1 mm, 100 μm, 50 μm from left to right. (**C**) Recording schematic showing photostimulation of oChIEF-expressing axon fibers of transfected PCs (*filled triangles*) and a whole-cell recording from non-transfected PCs (*empty triangles*) or FSINs (*empty circles*). A collimated DMD-coupled LED was used to confine the area of excitation (typically 3–4 μm in diameter) to a small region (*blue circle*) near the soma. (**D, E**) Representative traces for EPSCs averaged over 10 trials at each frequency (*left*) and average amplitudes of baseline-normalized EPSCs (*right*) during 20-pulse trains at frequencies from 5 to 40 Hz at PC-PC (*D*; n = 12, 9, 21, 10 cells for 5, 10, 20, 40 Hz, respectively) and PC-FSIN (*E*; n = 8, 9, 10, 10) synapses. Each data point was normalized to the average of the first EPSC. (**F**) Baseline-normalized amplitudes of steady-state EPSCs ($EPSC_{ss}$; *black symbols*) and synaptic efficacy ($EPSC_{ss} \times f$; *red symbols*) as a function of stimulation frequency (*f*) at PC–PC synapses. $EPSC_{ss}$ was measured from the average of last 5 EPSCs from the 20-pulse trains (n = 12, 9, 21, 10). (**G**) Paired pulse ratio (PPR) as a function of inter-spike intervals (n = 25, 9, 25, 22, 43 for 200, 100, 50, 25, 20 ms ISI, respectively) at PC-PC synapses. (**H**) $EPSC_{ss}$ and synaptic efficacy at PC-FSIN (n = 8, 9, 10, 10). (**I**) PPR at PC-FSIN (n = 8, 9, 10, 15, 34). *Gray symbols*, individual data.

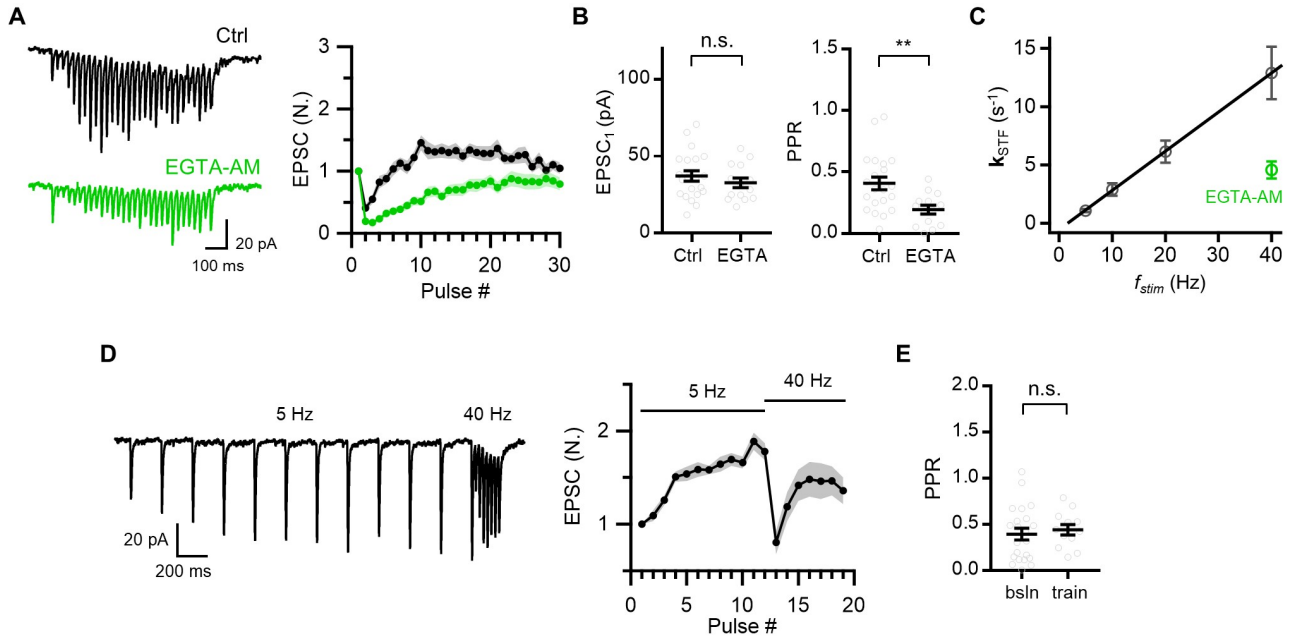

Figure 2. Delayed facilitation results from slow activation of Ca^{2+}-dependent vesicle replenishment at a constantly high vesicular fusion probability

(**A**) Representative traces (*left*) and mean baseline-normalized amplitudes (*right*) of EPSCs evoked by 30-pulse trains at 40 Hz in control (n = 21; *black*) and in the presence of 50 µM EGTA-AM (n = 14; *green*). (**B**) Mean values for the first EPSC amplitude ($EPSC_1$, *left*) and PPR (*right*) from the experiments displayed in (A). *Gray symbols*, individual data. (**C**) Plot of rate constants for short-term facilitation ($\mathbf{k}_{STF}$) as a function of stimulation frequency (f_{stim}), showing a linear relationship. The linear regression line (*black*) is shown fitted to $\mathbf{k}_{STF}$ values, estimated from Figure 1. (**D**) Representative EPSC traces (*left*) and average of baseline-normalized EPSCs (*right*) evoked by 12-pulse stimulation at 5 Hz, followed by 40 Hz 7-pulse train (n = 12). Note that slowly developing facilitation was converted to rapid facilitation after strong PPD. (**E**) Mean values for PPR at 40 Hz. The baseline PPR was reproduced from Figure 1G and the PPR during 5 Hz train was calculated as (13th EPSC) / (12th EPSC). *Gray symbols*, individual data. All statistical data are represented as mean ± S.E.M.; n.s. = not significant; **, $P < 0.01$; unpaired t-test.

39

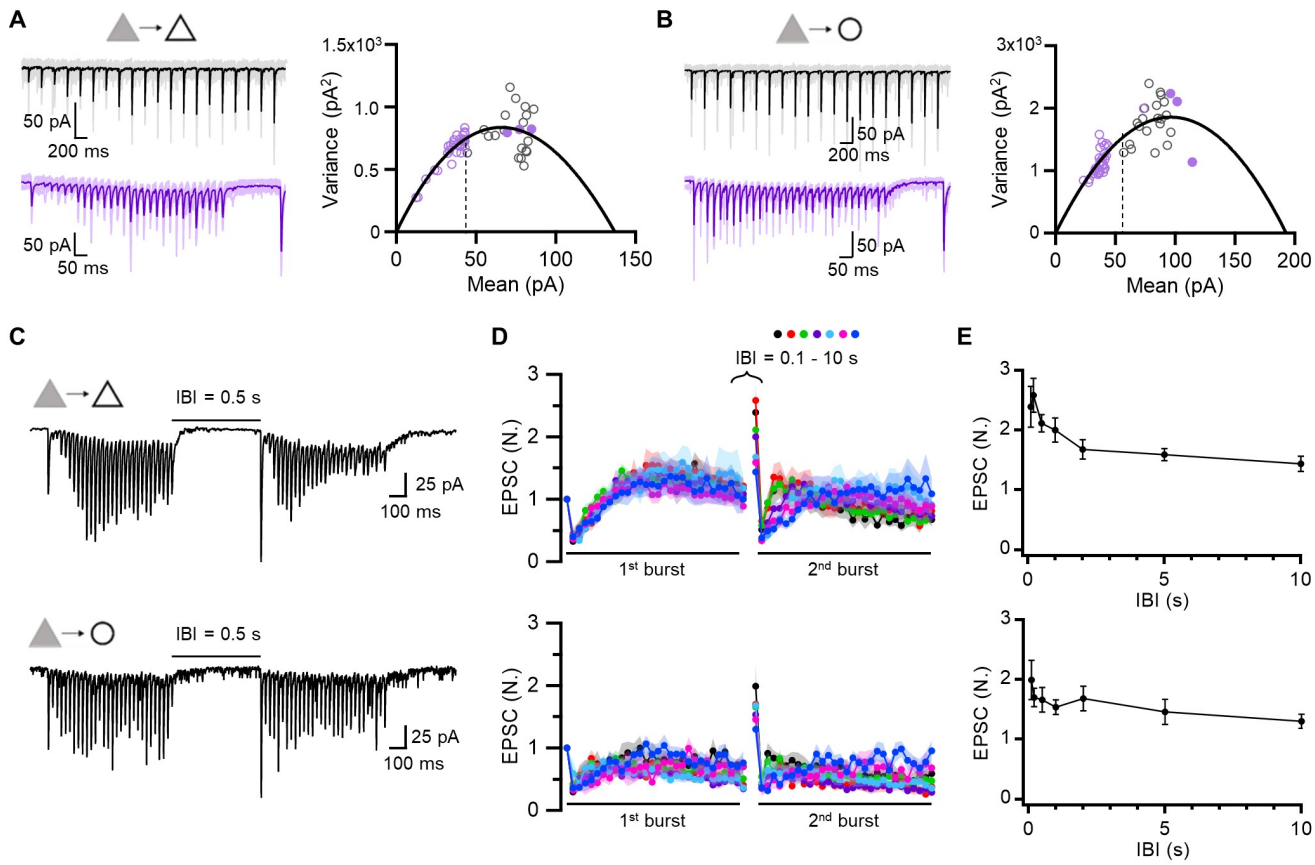

Figure 3. Low baseline occupancy of release sites and its increase during facilitation and post-tetanic augmentation

(**A, B**) *Left*, Representative EPSCs evoked by 5 and 40 Hz train stimulation (*black*, 5 Hz; *purple*, 40 Hz). *Right*, Variance-mean plots of EPSCs amplitude from averaged EPSCs recorded at PC-PC (A; n = 12, 17 for 5 and 40 Hz, respectively) and PC-FSIN (B; n = 8, 10) synapses. The data were fitted using multiple-probability fluctuation analysis (MPFA). Error bars are omitted for clarity. The 1st EPSC of 5 Hz train (*broken line*) was used to estimate the resting level of p_{occ}. *Filled circles* were measured from post-tetanic augmented EPSCs (*A*, n = 12, 12, 9; *B*, n = 7, 7, 7 for 0.1, 0.2, 0.5 s IBIs, respectively). (**C-E**) Post-tetanic augmentation (PTA) experiments at PC-PC (*top*) and PC-FSIN (*bottom*) synapses. (**C**) Representative traces for EPSCs evoked by double 40 Hz train stimulations separated by 0.5 s. (**D**) Mean baseline-normalized amplitudes of EPSCs evoked by double 40 Hz trains at different inter-burst intervals (IBIs, 0.1, 0.2, 0.5, 1, 2, 5, 10 s). *Upper*, PC-PC synapse (n = 12, 12, 21, 11, 11, 16, 11 from short to long IBIs,

53 respectively). *Lower*, PC-FSIN synapse (n = 10, 9, 8, 9, 9, 7, 9). (**E**) PTA time course. The
54 baseline-normalized amplitudes of 1st EPSC from the 2nd train were plotted as a function of
55 IBIs.
56
57

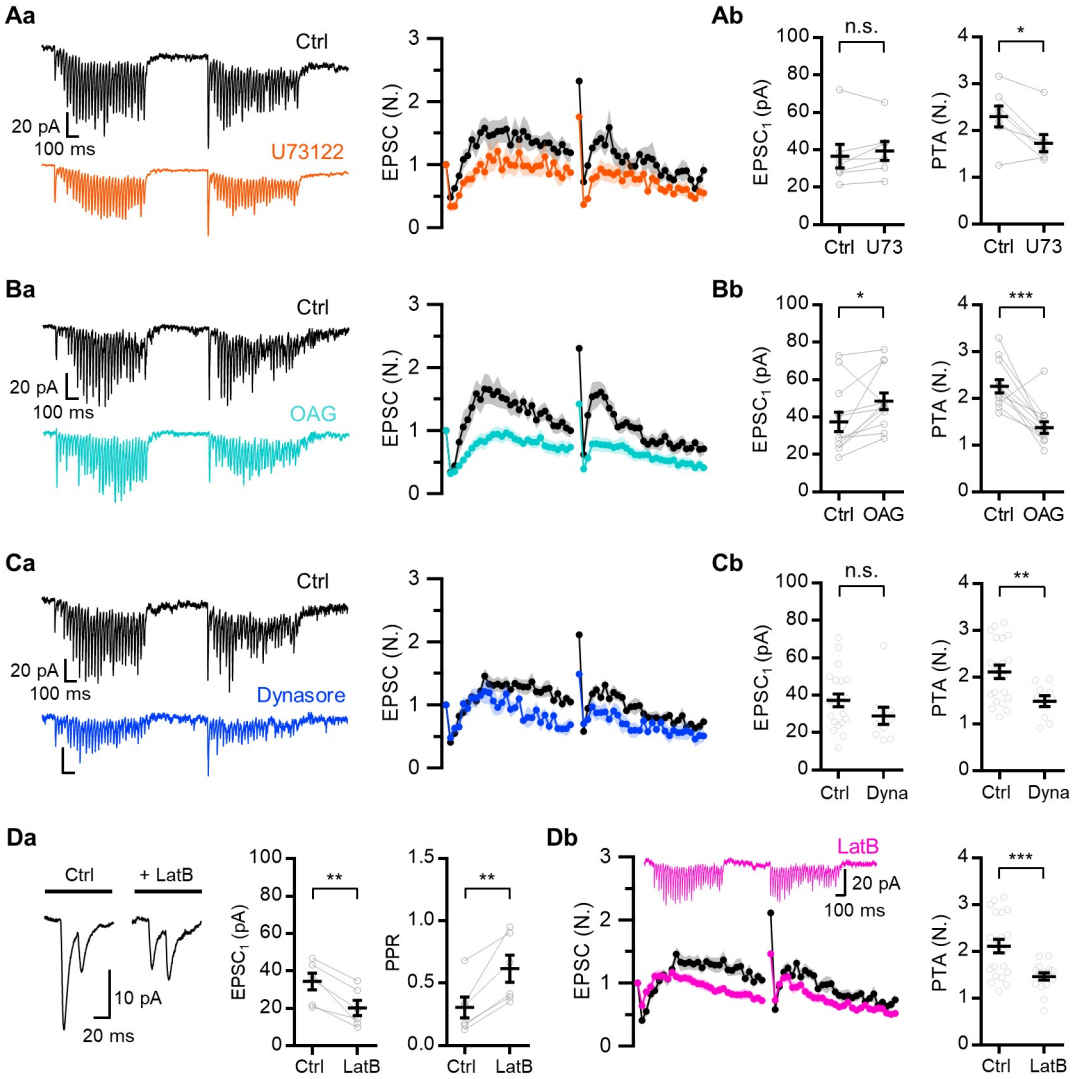

Figure 4. Pharmacological experiments reveal specific molecular mechanisms underlying vesicle loading processes

(**A-C**) (**a**) Representative EPSC traces (*left*) and mean baseline-normalized EPSCs (*right*) evoked by double 40 Hz train stimulations separated by 0.5 s inter-burst interval (IBI) in control and in the presence of 5 µM U73122 (*Aa*, n = 7, *orange*), 20 µM OAG (*Ba*, n = 12, *cyan*) or 100 µM dynasore (*Ca*, n = 10, *blue*). (**b**) Mean values for baseline EPSCs ($EPSC_1$, *left*) and augmentation (*right*) from the experiments shown in corresponding *a* panel. (**Da**) Representative EPSC traces evoked by paired pulses (*left*) and mean values for baseline EPSC amplitude (*middle*) and PPR (*right*) before and after applying 20 µM LatB (n = 6). (**Db**) Representative EPSC traces

(*left, upper*) and average of normalized EPSCs (*left, lower*) evoked by double 40 Hz train stimulation separated by 0.5 s in control (n = 21) and in 20 µM LatB conditions (n = 16; *pink*). *Right*, Mean values for augmentation in control and LatB conditions. *Gray symbols*, individual data. All statistical data are represented as mean ± S.E.M., *, $P < 0.05$; **, $P < 0.01$; ***, $P < 0.001$; unpaired or paired t-test; n.s. = not significant.

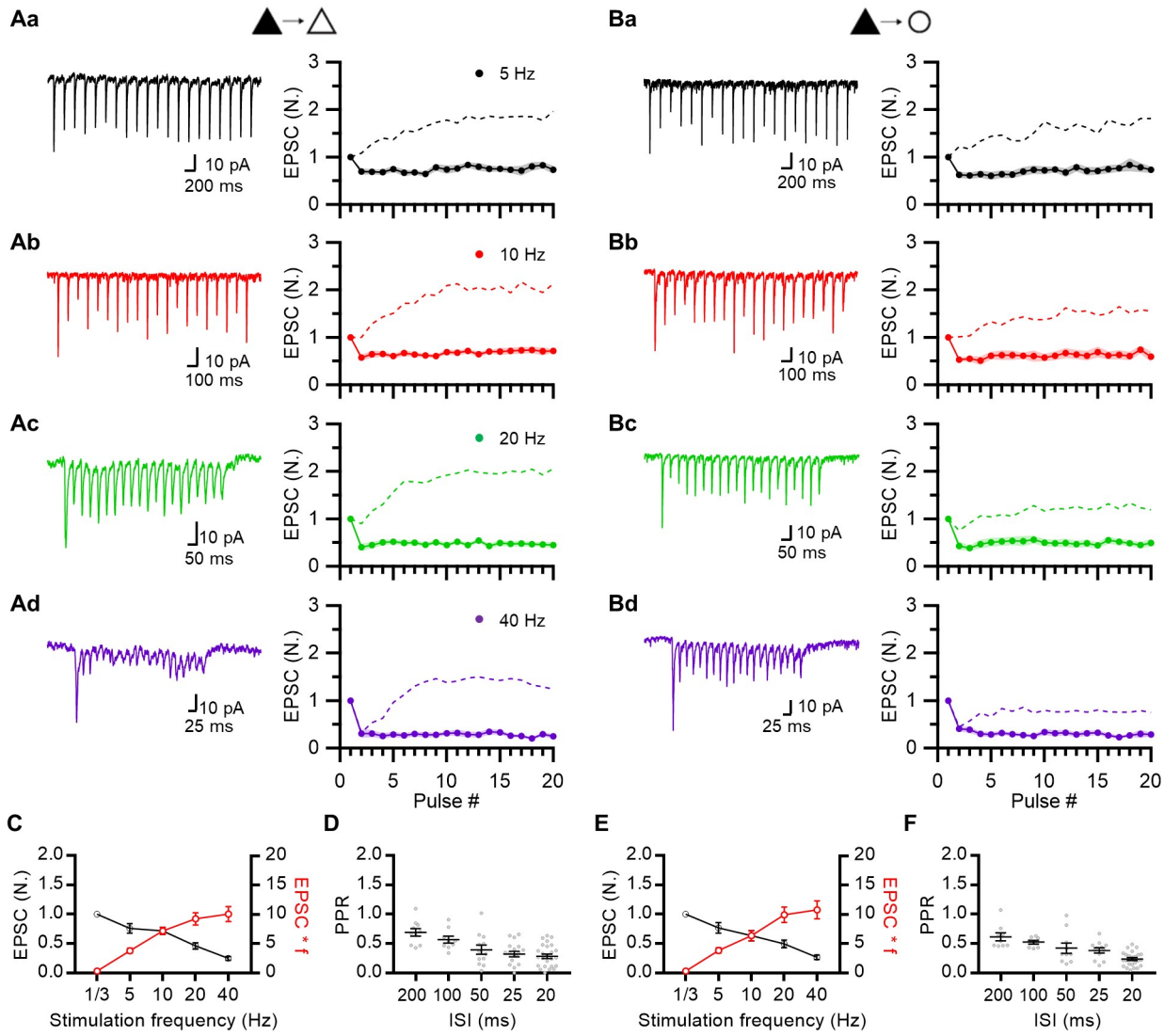

74 **Figure 5. STF at both types of local excitatory synapses is abolished by Syt7 KD**

75 (**A, B**) Representative EPSC traces (*left*) and mean baseline-normalized amplitudes of EPSCs
76 (*right*) evoked by 20-pulse trains at 5 to 40 Hz. STP was measured at PC-PC (*A*; n = 10, 9, 12,
77 9) and PC-FSIN (*B*; n = 9, 8, 10, 9) synapses, in which presynaptic Syt7 transcripts were
78 depleted (Syt7 KD). Syt7 KD pyramidal cells are indicated as *black triangles* on the top. For
79 comparison, STP in WT synapses is reproduced from Figure 1 (*dotted lines*). Same frequency
80 color codes were used as in Figure 1. (**C**) Baseline-normalized amplitudes of steady-state EPSC
81 ($EPSC_{ss}$; *black symbols*) and synaptic efficacy ($EPSC_{ss} \times f$; *red symbols*) as a function of

82 stimulation frequency (*f*) at PC-PC synapses. $EPSC_{ss}$ was defined as the average of last 5 EPSC
83 amplitudes from 20-pulse trains. (**D**) PPR as a function of inter-spike intervals (n = 10, 9, 12,
84 18, 26). (**E**) $EPSC_{ss}$ and synaptic efficacy at PC-FSIN synapses. (**F**) PPR at PC-FSIN synapses (n =
85 9, 8, 10, 12, 24). *Gray symbols*, individual data.
86
87

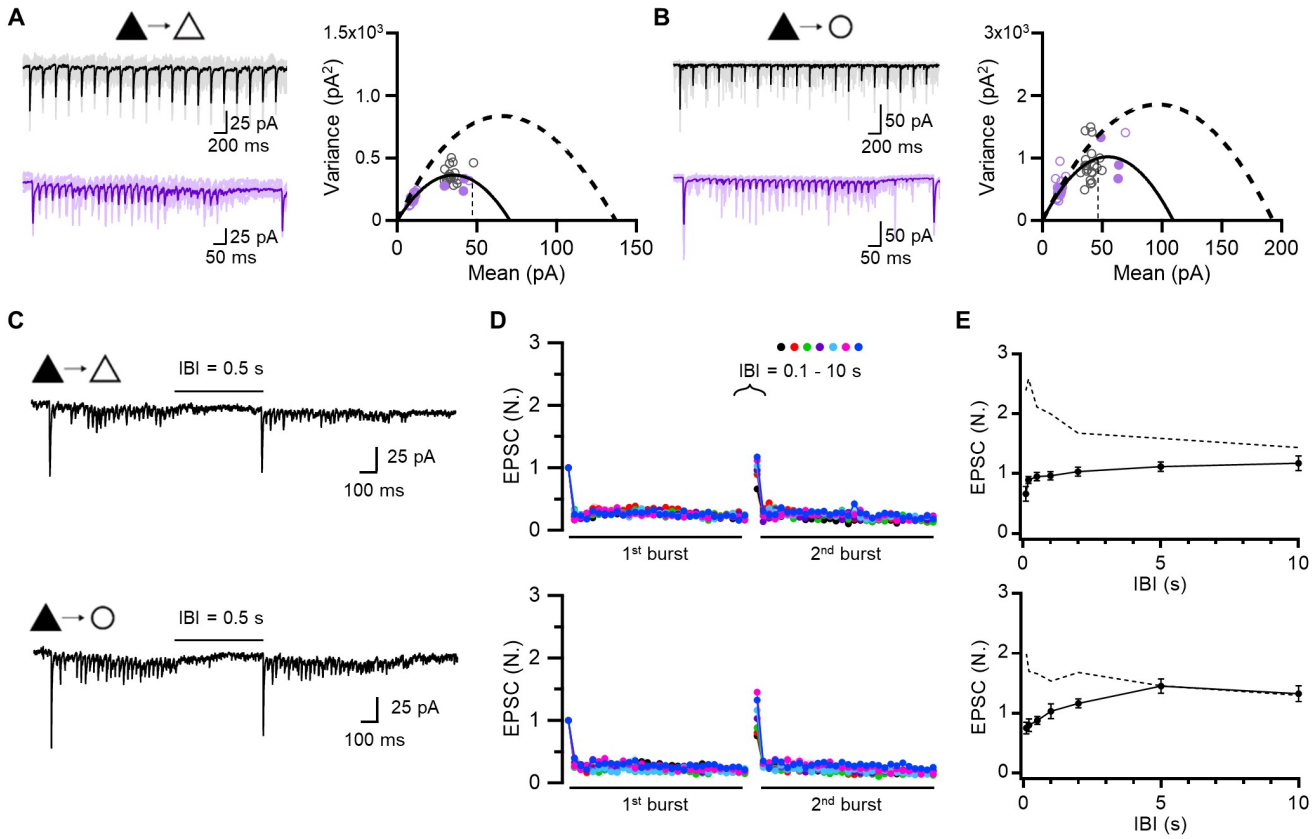

Figure 6. Syt7 KD synapses exhibit complementary changes in the number of release sites and their vesicle occupancy

(**A, B**) *Left*, Representative traces of EPSCs evoked by 5 and 40 Hz train stimulations (*black*, 5 Hz; *purple*, 40 Hz). *Right*, Variance-mean plots of EPSCs amplitude from averaged EPSCs recorded at PC-PC (*A*; n = 9, 15, 12, 10, 9) and PC-FSIN (*B*; n = 4, 14, 10, 9, 8) synapses in which presynaptic Syt7 has been knocked down. The data were fitted using MPFA and error bars are omitted for clarity. The mean 1st EPSC amplitude of 5 Hz train (*dotted line*) was used for estimation of baseline p_{occ}. *Broken lines* indicate MPFA fits to variance-mean plot of WT synapses reproduced from Figure 2. (**C-E**) Recovery experiments at PC-PC (*top*) and PC-FSIN (*bottom*) synapses in which presynaptic Syt7 was knocked-down. (**C**) Representative EPSCs evoked by double 40 Hz train stimulations separated by 0.5 s. (**D**) Mean baseline-normalized amplitudes of EPSCs evoked by double 40 Hz trains at PC-PC (n = 12, 10, 9, 9, 10, 9, 8) and PC-FSIN (n = 10, 9, 10, 11, 8, 9, 10) synapses at different interburst intervals (IBIs). (**E**) PTA time

course. Baseline-normalized amplitudes of 1st EPSC from the 2nd burst were plotted as a function of various IBIs. *Dotted lines* indicate augmented EPSCs in the WT reproduced from Figure 2.

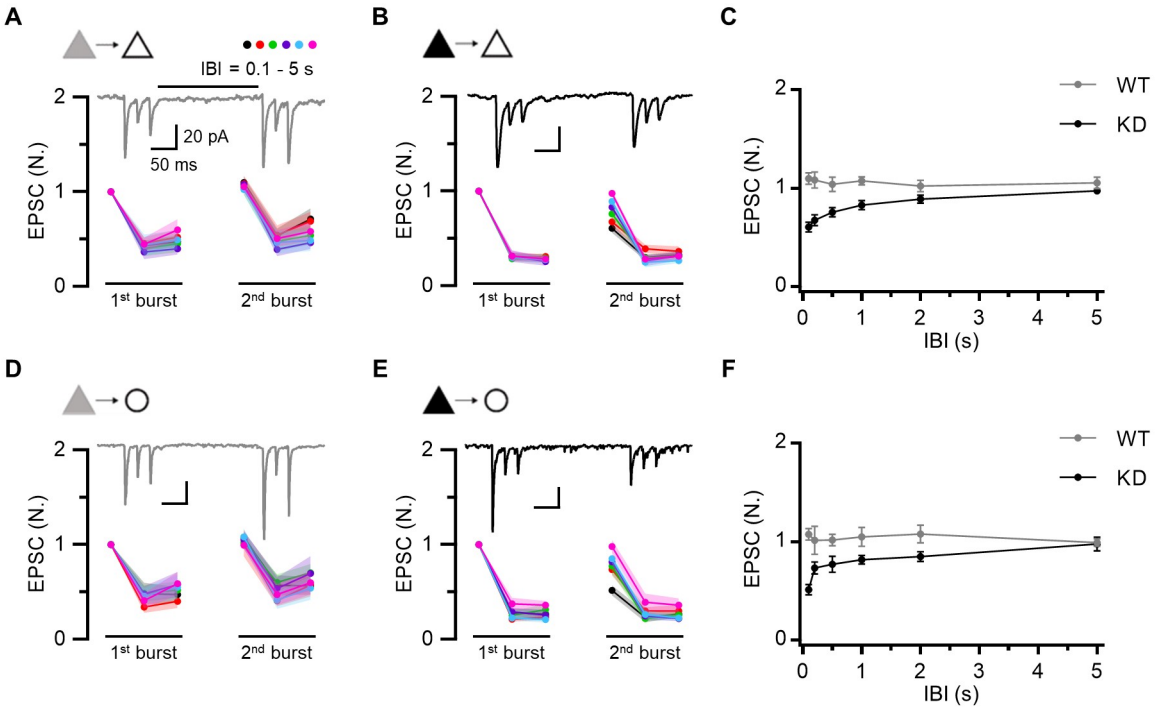

106 **Figure 7. Recovery of TS vesicles following depletion is accelerated by Syt7**

107 (**A-C**). Recovery experiments at PC-PC synapses in WT (*A*) and Syt7 KD (*B*). Mean baseline-
108 normalized amplitudes of EPSCs evoked by two consecutive 3-pulse 40 Hz trains in WT (n =
109 16, 13, 11, 11, 11, 9 from short to long IBIs, respectively) and KD (n = 13, 11, 12, 8, 10, 11)
110 synapses at different IBIs (0.1, 0.2, 0.5, 1, 2, 5 s). *Inset*, representative traces of EPSCs evoked
111 by two consecutive 3-pulse 40 Hz train stimulations separated by 0.5 s. (**D-F**). Recovery
112 experiments at PC-FSIN synapses in WT (*D*) and Syt7 KD (*E*). Mean baseline-normalized
113 amplitudes of EPSCs evoked by two consecutive 3-pulse 40 Hz trains in WT (n = 9, 11, 11, 9,
114 10, 13) and KD (n = 9, 12, 9, 7, 10, 9) synapses at different IBIs. *Inset*, representative traces of
115 EPSCs evoked by two consecutive 3-pulse 40 Hz train stimulations separated by 0.5 s. (**C, F**)
116 Recovery time course. Baseline-normalized amplitudes of 1st EPSC from the 2nd burst were
117 plotted as a function of various IBIs.

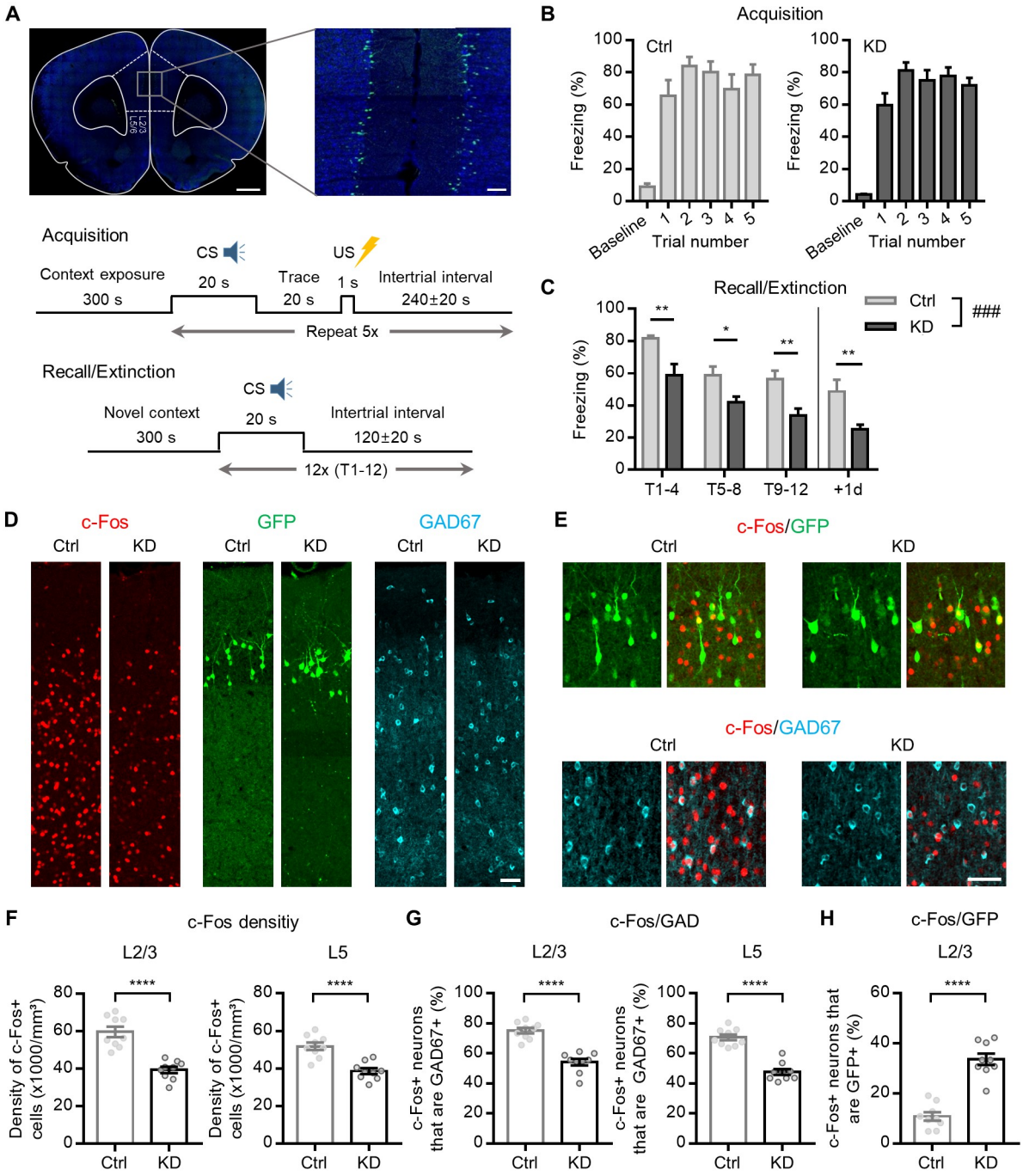

118 **Figure 8. Behavioral effects of Syt7 deficiency in L2/3 PCs of the mPFC**

119 (**A**) *Top*, Representative images showing bilateral expression of U6-GFP in L2/3 of PCs after
120 IUE at E17.5. Scale bar: 1 mm, 100 µm. *Bottom*, Schematic of trace fear conditioning and
121 extinction (tone test) protocol. (**B**) Freezing behavior of control (expressing scrambled shRNA,
122 *Scr*) and Syt7 KD rats during acquisition of tFC. (**C**) Freezing ratio during tone tests on following

days. Data are shown as average freezing during T1–T4, T5–T8, or T9–T12 (T, trials). The freezing on T1-T4 was significantly lower in KD rats suggesting that formation of trace memory was impaired in Syt7 KD rats (n = 10, 11 for Ctrl and KD, respectively; P = 0.0007, F(1, 19) = 16.43, two-way repeated measures ANOVA; P = 0.0064, 0.0211, 0.0064, 0.0064; Holm-Sidak test). (**D**) Representative images of c-Fos immunoreactivity in the prelimbic cortex of control or Syt7 KD rats 90 min after tFC acquisition. c-Fos (*left*, *red*, Cy5) and GAD67 (*right*, *cyan*, Cy3) were immunostained in the same brain slice expressing U6-GFP (*middle*; *green*). Scale bar, 50 µm. (**E**) Exemplar images of c-Fos positive neurons expressing GFP (*top*) or GAD67 (*bottom*) in control (*left*) or Syt7 KD rats (*right*). Scale bar, 50 µm. (**F-H**) Effects of Syt7 KD on c-Fos density (*F*) and percentage of c-Fos positive neurons co-labeled with GAD67 (*G*) or GFP (*H*) in L2/3 or L5 of prelimbic cortex (n = 9, 9 for Ctrl and KD, respectively). *Open symbols*, individual data. All statistical data are represented as mean ± S.E.M.; ****, P＜0.0001; unpaired t-test.

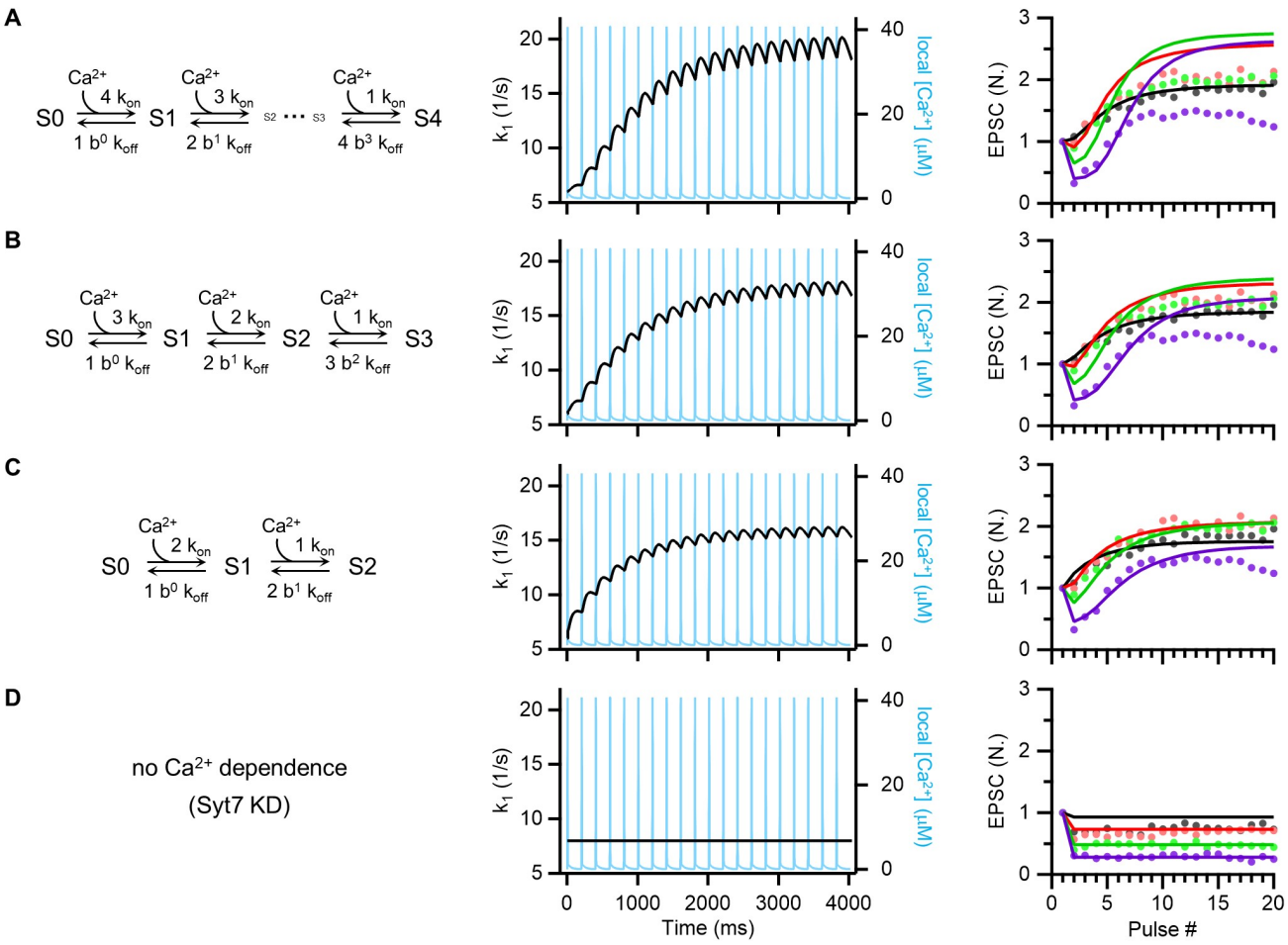

137 **Figure 9. STP model in light of known Ca^{2+} binding kinetics of Syt7**

138 (**A-D**) *Left*, Schematic of allosteric calcium binding to Syt7. The number of Ca^{2+} bound to Syt7
139 was denoted as # in 'S#' in the reaction scheme. k_{on} = 7/μM/s, k_{off} = 10/s. *Middle*, Simulated
140 changes of k_1 (*black*) in response to 5 Hz train of Ca^{2+} transients (*light blue traces*). The priming
141 step of the simple refilling model was assumed to be catalyzed by full Ca^{2+}-bound from of Syt7.
142 Accordingly, Ca^{2+}-dependent increase in k_1 was calculated as $K_{1,max}$ multiplied by a fraction of
143 full Ca^{2+}-bound form of Syt7. We assumed that local $[Ca^{2+}]_i(t)$ follows a Gaussian function: $(1/\sigma$
144 $\sqrt{2\pi})\exp[-(t-t_p)^2/2\sigma^2]$, in which t_p = 0.25 ms and σ = 0.085 ms. *Right*, Fits of the Syt7 model to
145 the STP data. To fit this model to the STP data, $K_{1,max}$ was set to 300/s (*A*), 220/s (*B*), and 180/s
146 (*C*). Cooperativity factor (*b*) was set to 0.35 (*A*), 0.2 (*B*), and 0.05 (*C*). k_1 is set to be constant
147 for Syt7 KD (*D*). Same frequency color codes were used as in Figure 1.